Genetic requirement of *dact1/2* to regulate noncanonical Wnt signaling and *calpain 8* during embryonic convergent extension and craniofacial morphogenesis

Shannon H. Carroll[1,2,3,], Sogand Schafer[1,2], Kenta Kawasaki[2,3], Casey Tsimbal[2,3], Amélie M. Julé[4], Shawn A. Hallett[2,3], Edward Li[2] and Eric C. Liao[1,2,3]

[1]Center for Craniofacial Innovation, Children's Hospital of Philadelphia Research Institute, Children's Hospital of Philadelphia, PA 19104, USA.

[2]Division of Plastic and Reconstructive Surgery, Department of Surgery, Children's Hospital of Philadelphia, PA 19104, USA.

[3]Shriners Hospital for Children, Tampa, FL 33607, USA

[4] Department of Biostatistics, Harvard T.H. Chan School of Public Health, Boston, MA 02115, USA

Abstract

Wnt signaling plays a crucial role in the early embryonic patterning and development, to regulate convergent extension during gastrulation and the establishment of the dorsal axis. Further, Wnt signaling is a crucial regulator of craniofacial morphogenesis. The adapter proteins Dact1 and Dact2 modulate the Wnt signaling pathway through binding to Disheveled. However, the distinct relative functions of Dact1 and Dact2 during embryogenesis remain unclear. We found that *dact1* and *dact2* genes have dynamic spatiotemporal expression domains that are reciprocal to one another and to *wnt11f2*, that suggest distinct functions during zebrafish embryogenesis. We found that both *dact1* and *dact2* contribute to axis extension, with compound mutants exhibiting a similar convergent extension defect and craniofacial phenotype to the *wnt11f2* mutant. Utilizing single-cell RNAseq and *gpc4* mutant that disrupts noncanonical Wnt signaling, we identified *dact1/2* specific roles during early development. Comparative whole transcriptome analysis between wildtype, *gpc4* and *dact1/2* mutants revealed a novel role for *dact1/2* in regulating the mRNA expression of the classical calpain *capn8*. Over-expression of *capn8* phenocopies *dact1/2* craniofacial dysmorphology. These results identify a previously unappreciated role of *capn8* and calcium-dependent proteolysis during embryogenesis. Taken together, our findings highlight the distinct and overlapping roles of *dact1* and *dact2* in embryonic craniofacial development, providing new insights into the multifaceted regulation of Wnt signaling.

Introduction

Wnt signaling is a crucial regulator of embryogenesis through its regulation of body axis patterning, cell fate determination, cell migration, and cell proliferation (Logan and Nusse 2004, Steinhart and Angers 2018, Mehta, Hingole et al. 2021). Current mechanistic understanding of Wnt signaling during embryogenesis includes an extensive catalog of ligands, receptors, co-receptors, adaptors, and effector molecules (Clevers and Nusse 2012, Niehrs 2012, Loh, van Amerongen et al. 2016, Mehta, Hingole et al. 2021). The intricate spatiotemporal integration of Wnt signaling combinations is an important focus of developmental biology and tissue morphogenesis (Petersen and Reddien 2009, Clevers and Nusse 2012, Loh, van Amerongen et al. 2016, Wiese, Nusse et al. 2018). Disruptions of Wnt signaling-associated genes lead to several congenital malformations which often affect multiple organ systems given their pleotropic developmental functions (Hashimoto, Morita et al. 2014, Shi 2022). Craniofacial anomalies are among the most common structural congenital malformations and genes in the Wnt signaling pathway are frequently implicated (Ji, Hao et al. 2019, Reynolds, Kumari et al. 2019, Huybrechts, Mortier et al. 2020). The roles of certain Wnt signaling components may change in different temporal and spatial contexts, requiring detailed developmental and genetic analyses.

Genetic approaches in zebrafish have identified a number of key Wnt regulators of early development, with gastrulation and craniofacial phenotypes (Brand, Heisenberg et al. 1996, Hammerschmidt, Pelegri et al. 1996, Heisenberg, Brand et al. 1996, Piotrowski, Schilling et al. 1996, Solnica-Krezel, Stemple et al. 1996, Schilling and Le Pabic 2009).

The *silberblick (slb)* mutant, later identified as a *wnt11f2* mutant allele, exhibited gastrulation and midline craniofacial phenotypes that encompassed aspects of multiple mutant classes (Heisenberg, Brand et al. 1996). During early segmentation in the somite stage, the *wnt11f2* mutant developed a shortened anterior-posterior axis and partially fused eyes (Heisenberg, Brand et al. 1996). Subsequently, as the cranial prominences converge and the ethmoid plate (EP) formed, instead of a fan-shaped structure observed in wildtype embryos, the *wnt11f2* mutant formed a rod-like EP with significant deficiency of the medio-lateral dimension (Heisenberg, Brand et al. 1996, Heisenberg and Nusslein-Volhard 1997). Another mutant kny*pek (kny)*, identified as having a nonsense mutation in *gpc4*, an extracellular Wnt co-receptor, was identified as a gastrulation mutant that also exhibited a shortened body axis due to a defect in embryonic convergent extension (CE) (Solnica-Krezel, Stemple et al. 1996). In contrast to the *slb*/*wnt11f2 mutant*, the *gpc4* mutant formed an EP that is wider in the medio-lateral dimension than the wildtype, in the opposite end of the EP phenotypic spectrum compared to *wnt11f2* (Topczewski, Sepich et al. 2001, Rochard, Monica et al. 2016). These observations beg the question how defects in early patterning and CE of the embryo may be associated with later craniofacial morphogenesis. The observation that *wnt11f2* and *gpc4* mutant share similar CE dysfunction and axis extension phenotypes but contrasting craniofacial morphologies was previously pondered (Heisenberg and Nusslein-Volhard 1997). This observation supports a hypothesis that CE mechanisms regulated by these Wnt pathway genes are specific to the temporal and spatial contexts during embryogenesis. As such, there may be Wnt signaling modifiers that act in specific temporal windows during development.

Dact (aka Frodo, Dapper) are scaffolding proteins that were identified to regulate Dishevelled (Dvl)-mediated Wnt signaling, both positively and negatively (Cheyette, Waxman et al. 2002, Gloy, Hikasa et al. 2002, Waxman, Hocking et al. 2004, Gao, Wen et al. 2008, Wen, Chiang et al. 2010, Ma, Liu et al. 2015, Lee, Cheong et al. 2018). Dact proteins bind directly to Dvl (Gloy, Hikasa et al. 2002, Brott and Sokol 2005, Lee, Cheong et al. 2018) and have been found to interact with and inhibit members of TGFβ and Nodal signaling pathways (Zhang, Zhou et al. 2004, Su, Zhang et al. 2007, Meng, Cheng et al. 2008, Kivimae, Yang et al. 2011). In chick and Xenopus, *Dact2* and *Dact1* are expressed (respectively) in the neural folds during neural crest delamination and these were found to be important in epithelial-mesenchymal transition (EMT), Wnt, and Tgfβ signaling (Hikasa and Sokol 2004, Schubert, Sobreira et al. 2014, Rabadan, Herrera et al. 2016). In mouse embryos, Dact1 expression was reported predominantly in mesodermal tissues as well as ectodermal-derived tissues (Hunter, Hikasa et al. 2006) and ablation of Dact1 resulted in defective EMT and morphogenesis at the primitive streak and subsequent posterior defects (Wen, Chiang et al. 2010). Mouse embryonic Dact2 expression has been described in the oral epithelium (Li, Florez et al. 2013) and ablation of *Dact2* causes increased cell proliferation (Li, Florez et al. 2013) and re-epithelialization in mice (Meng, Cheng et al. 2008) as well as zebrafish (Kim, Kim et al. 2020).

Previous experiments using morpholinos to disrupt *dact1* and *dact2* in zebrafish found *dact1* morphants to be slightly smaller and to develop a normal body. In contrast, *dact2*

morphants were found to phenocopy described zebrafish gastrulation mutants, with impaired CE, shortened body axis, and medially displaced eyes. Importantly, prior work using morpholino-mediated gene disruption of *dact1* and *dact2* did not examine craniofacial morphogenesis except to analyze *dact1* and *dact2* morphants head and eye shapes from light microscopy (Waxman, Hocking et al. 2004). These experiments were carried out at a time when morpholino was the accessible tool of gene disruption (Nasevicius and Ekker 2000, Corey and Abrams 2001, Heasman 2002). Since CRISPR/Cas9 targeted gene mutagenesis became popularized, many reports of germline mutant phenotypes being discrepant from prior morpholino studies warranted revisiting many of the prior work (Kok, Shin et al. 2015) and careful interpretation given the caveats of each technology (Morcos, Vincent et al. 2015, Rossi, Kontarakis et al. 2015). More recently, a zebrafish CRISPR/Cas9 genetic *dact2* mutant has been generated and studied, but unlike in the *dact2* morphant, no developmental phenotypes were described (Kim, Kim et al. 2020).

Here we investigated the genetic requirement of *dact1* and *dact2* during embryogenesis and craniofacial development, using germline mutant alleles generated by CRISPR-targeted mutagenesis. We found an early developmental role for *dact1* and *dact2* during gastrulation and body axis elongation. We also characterized the resulting craniofacial defect in the *dact1/2* compound mutants. Differential single-cell RNA sequencing between wildtype, *dact1/2,* and *gpc4* mutants revealed distinct transcriptome profiles and the discovery of *calpain 8* (*capn8)* calcium-dependent protease to be ectopically

expressed in the *dact1/2* mutants and functions to modify Wnt signaling and craniofacial morphogenesis.

Results

dact1 and *dact2* have distinct expression patterns throughout embryogenesis

To determine the spatiotemporal gene expression of *dact1* and *dact2* during embryogenesis we performed wholemount RNA *in situ* hybridization (ISH) across key time points (Fig. 1). Given that the described craniofacial phenotypes of the *dact2* morphant and the *wnt11f2* mutant are similar (Heisenberg and Nusslein-Volhard 1997, Waxman, Hocking et al. 2004), we also performed *wnt11f2* ISH to compare to *dact1* and *dact2* expression patterns.

During gastrulation at 8 hours post-fertilization (hpf; 75% epiboly), some regions of *dact1* and *dact2* gene expression were shared and some areas are distinct to each *dact* gene (Fig. 1A). Further, *dact* gene expression was distinct from *wnt11f2* in that *wnt11f2* expression was not detected in the presumptive dorsal mesoderm. Transcripts of *dact1*, *dact2,* and *wntllf2* were all detected in the blastoderm margin, as previously described (Gillhouse, Wagner Nyholm et al. 2004). Transcripts of *dact2*, and to a lesser extent *dact1*, were also detected in the prechordal plate and chordamesoderm (Fig. 1A). Additionally, *dact2* gene expression was concentrated in the shield and presumptive organizer or Nieuwkoop center along with *wnt11f2*. This finding is consistent with previously described expression patterns in zebrafish and supports a role for *dact1 and dact2* in mesoderm induction and *dact2* in embryo dorsalization (Thisse 2001, Gillhouse, Wagner Nyholm et al. 2004, Muyskens and Kimmel 2007, Oteiza, Koppen et al. 2010). At the end of gastrulation and during somitogenesis the differences in the domains of *dact1* and *dact2* gene expressions became more distinct (Fig. 1B,C). At tailbud stage, *dact1* transcripts were detected in the trunk and the posterior paraxial

mesoderm, whereas *dact2* transcripts were detected in the anterior neural plate, notochord, and tailbud, similar to *wnt11f2* gene expression. However, *dact2* was unique in that its expression demarcated the anterior border of the neural plate. As *dact2* morphants exhibited a craniofacial defect with medially displaced eyes and midfacial hypoplasia (Waxman, Hocking et al. 2004), we examined *dact1* and *dact2* expression in the orofacial tissues. At 24 hpf we found some overlap but predominantly distinct expression patterns of *dact1* and *dact2* with *dact1* being more highly expressed in the pharyngeal arches and *dact2* being expressed in the midbrain/hindbrain boundary. Both *dact1* and *dact2* appeared to be expressed in the developing oral cavity. At 48 hpf *dact1* expression is consistent with expression in the developing craniofacial cartilage elements, while *dact2* expression appears within the developing mouth. The distinct cellular expression profiles of *dact1* and *dact2* were more clear in histological sections through the craniofacial region at 72 hpf. Utilizing RNAscope *in situ* hybridization, we found that *dact2* and the epithelial gene *irf6* were co-expressed in the surface and oral epithelium that surround the cartilaginous structures (Fig. 1D). This is in contrast to *dact1* which was expressed in the developing cartilage of the anterior neurocranium/EP and palatoquadrate of the zebrafish larvae (Fig. 1D).

We examined the differences in expression pattern between *dact1* and *dact2* using Daniocell single-cell sequencing data (Farrell, Wang et al. 2018) (Fig. S1). During embryogenesis, *dact2* was more highly expressed in anterior structures including cephalic mesoderm and neural ectoderm while *dact1* was more highly expressed in mesenchyme and muscle (Fig. S1). We also utilized this tool to compare *dact1* and *dact2* expression to *wnt11f2* and *gpc4* expression, known noncanonical Wnt pathway

members with craniofacial phenotypes (Heisenberg, Brand et al. 1996, Solnica-Krezel, Stemple et al. 1996, Heisenberg and Nusslein-Volhard 1997). In general, we found *dact1* spatiotemporal gene expression to be more similar to *gpc4* while *dact2* gene expression was more similar to *wnt11f2*. These results of shared but also distinct domains of spatiotemporal gene expression of *dact1* and *dact2* suggest that the *dact* paralogs may have some overlapping developmental functions while other roles are paralog specific.

dact1 and _dact2_ contribute to axis extension and _dact1/2_ compound mutants exhibit a convergent extension defect

dact1 and *dact2* are known to interact with *disheveled* and regulate non-canonical Wnt signaling (Gloy, Hikasa et al. 2002, Waxman, Hocking et al. 2004, Gao, Wen et al. 2008, Wen, Chiang et al. 2010, Ma, Liu et al. 2015, Lee, Cheong et al. 2018) and we have previously described the craniofacial anomalies of several zebrafish Wnt mutants (Dougherty, Kamel et al. 2012, Kamel, Hoyos et al. 2013, Rochard, Monica et al. 2016, Ling, Rochard et al. 2017, Alhazmi, Carroll et al. 2021). Previous work investigated the effect of *dact1* and *dact2* disruption during zebrafish embryogenesis using morpholinos and reported morphant phenotypes in embryonic axis extension and eye fusion (Waxman, Hocking et al. 2004). However, the limitations associated with morpholino-induced gene disruption (Kok, Shin et al. 2015, Morcos, Vincent et al. 2015, Rossi, Kontarakis et al. 2015) and the fact that craniofacial morphogenesis was not detailed for the *dact1* and *dact2* morphants, warranted the generation of mutant germline alleles (Fig. S2). We created a *dact1* mutant allele (22 bp deletion, hereafter

dact1-/-) and a *dact2* mutant allele (7 bp deletion, hereafter *dact2-/-*), both resulting in a premature stop codon and presumed protein truncation (Fig. S2A,B). Gene expression of *dact1* and *dact2* was measured in pooled *dact1-/-*, *dact2-/-,* and *dact1/2-/-* embryos (Fig. S2C). We found a decrease in *dact1* mRNA and no change in *dact2* mRNA levels in the respective CRISPR mutants. We hypothesize that *dact2* mRNA levels are maintained in the *dact2-/-* mutant due to the relative 3' position of the deletion. In the *dact2-/-* embryos we found a slight increase in *dact1* mRNA levels, suggesting a possible compensatory effect of dact2 disruption. The specificity of the gene disruption was demonstrated by phenotypic rescue of the rod-like EP with the injection of *dact1* or *dact2* mRNA. Injection of *dact1* mRNA or *dact2* mRNA or in combination decreased the percentage of rod-like EP phenotype from near the expected 25% (35% actual) to 2-7% (Fig. S2D,E).

Analysis of compound *dact1* and *dact2* heterozygote and homozygote alleles during late gastrulation and early segmentation time points identified embryonic axis extension anomalies (Fig. 2A,B). *dact1-/-* or *dact2-/-* homozygotes develop to be phenotypically normal and viable. However, at 12 hpf, *dact2-/-* single mutants have a significantly shorter body axis relative to wildtype. In contrast, body length shortening phenotype was not observed in *dact1-/-* homozygotes. Compound heterozygotes of *dact1+/-*; *dact2+/-* also developed normally but exhibited shorter body axis relative to wildtype. The most significant axis shortening occurred in *dact1-/-; dact2-/-* double homozygotes with a less severe truncation phenotype in the compound heterozygote *dact1+/-; dact2-/-* (Fig. 2A,B). Interestingly, these changes in body axis extension do not preclude the compound heterozygous larvae from reaching adulthood, except in the

dact1-/-; dact2-/- double homozygotes which did not survive from larval to juvenile stages.

Body axis truncation has been attributed to impaired CE during gastrulation (Tada and Heisenberg 2012). To delineate CE hallmarks in the *dact1*-/-;*dact2*-/- mutants, we performed wholemount RNA ISH detecting genes that are expressed in key domains along the body axis. At bud stage, *dact1-/-; dact2-/-* embryos demonstrate bifurcated expression of *pax2a* and decreased anterior extension of *gsc* expression, suggesting impaired midline convergence and anterior extension of the mesoderm (Fig. 2C). At the 1-2 somite stage, *zic1*, *pax2a* and *tbx6* are expressed in neural plate, prospective midbrain and the tailbud, respectively, in both the wildtype and *dact1-/-; dact2-/-* embryos. However, the spacing of these genes clearly revealed the shortening of the anteroposterior body axis in the *dact1-/-; dact2-/-* embryos. Midline convergence is decreased and the anterior border of the neural plate (marked by *zic1* expression) was narrower in the *dact1-/-; dact2-/-* embryos (Fig. 2D). At the 10-somite stage (ss), *dact1-/-; dact2-/-* embryos demonstrated decreased spacing between *ctslb1* and *pax2a* gene expression, suggesting impaired lengthening of the anterior portion of the embryo. Detection of muscle marker *myo1d* in the *dact1-/-; dact2-/-* embryos delineated impaired posterior lengthening as well as reduced somitogenesis, evidenced by the decreased number of somites (Fig. 2E). These data point to impaired CE of the mesoderm in *dact1-/-; dact2-/-* double mutants, which resulted in a shorter body axis. The aberrant CE and axis extension in the *dact1*-/-;*dact2*-/- phenotypes were similar to findings in other Wnt mutants, such as *slb* and *kyn* (Heisenberg, Tada et al. 2000, Topczewski, Sepich et al. 2001) in that the body axis is truncated upon segmentation.

***dact1/dact2* compound mutants exhibit axis shortening and craniofacial dysmorphology**

Given the defective converge phenotype and shortened axis in the *dact* mutants during gastrulation, we examined the fish at 4 dpf for axis defects and for evidence of defective morphogenesis in the craniofacial cartilages. Craniofacial morphology is an excellent model for studying CE morphogenesis as many craniofacial cartilage elements develop through this cellular mechanism (Kamel, Hoyos et al. 2013, Mork and Crump 2015, Sisson, Dale et al. 2015, Rochard, Monica et al. 2016). No craniofacial phenotype was observed in *dact1* or *dact2* single mutants (data not shown). However, in-crossing to generate *dact1-/-; dact2-/-* compound homozygotes resulted in dramatic craniofacial malformation (Fig. 3). Specificity of this phenotype to *dact1/2* was confirmed via rescue with *dact1* or *dact2* mRNA injection (Fig. S1). The *dact1-/-;dact2-/-* mutant embryos exhibited fully penetrant midfacial hypoplasia (Fig. 3A) however the degree of eye field convergence in the midline varied between individuals. The forebrain protruded dorsally and the mouth opening and ventral cartilage structures were displaced ventrally (Fig. 3A). Alcian blue staining of cartilage elements revealed severe narrowing of the EP into a rod-like structure in 100 percent of double mutants, while the ventral cartilage elements were largely unaffected (Fig. 3B). Notably the trabeculae extending posteriorly from the EP and the rest of the posterior neurocranium exhibit wildtype morphology in *dact1/2*. This *dact1-/-;dact2-/-* double mutant phenotype is highly similar to that described for *wnt11f2* (*slb*) mutants, a key regulator of non-canonical Wnt signaling and CE (Kimmel, Miller et al. 2001).

As axis lengthening was found to be affected by loss of *dact1* and *dact2* (Fig. 2A) we measured body length in 5 dpf *dact1/2* compound mutants. Using the length of the vertebral spine as a measure of body length we found a trend (p=0.06) towards an effect of *dact1* and *dact2* on shortening of the body length. Similar to axis length during gastrulation/segmentation, the shortening was most pronounced in *dact1-/-; dact2-/-* double homozygous mutants versus wildtype clutch-mates (Fig. 3C, Fig. S3A,B).

As *wnt11f2* signals via disheveled and since dact proteins are known to interact with disheveled (Wong, Bourdelas et al. 2003, Zhang, Gao et al. 2006, Kivimae, Yang et al. 2011), it is suspected that dact has a role in wnt11f2 signaling. Combinatorial gene disruption with morpholinos showed that *dact2* morpholino exasperated the *wnt11* morpholino midfacial/eye fusion defect (Waxman, Hocking et al. 2004). We hypothesized that the shared phenotypes between *wnt11f2* and *dact1/2* mutants point to these genes acting in the same signaling pathway. To test for genetic epistasis between *wnt11f2*, *dact1,* and *dact2* genes we generated *wnt11f2-/-; dact1-/-; dact2-/-* triple homozygous mutants. If *wnt11f2* and *dact1/2* had independent developmental requirements, the *wnt11f2-/-; dact1-/-; dact2-/-* mutant may exhibit a phenotype distinct from *wnt11f2-/-* or *dact1-/-; dact2-/-* mutants. We found that the *wnt11f2-/-; dact1-/-; dact2-/-* triple homozygous mutant phenotype of the linear rod-like EP was the same as the *wnt11f2-/-* mutant or *dact1-/-;dact2-/-* double mutant, without exhibiting additional or neo-phenotypes in the craniofacial cartilages or body axis (Fig. 3D,E). This result supports *dact1 and dact2* acting downstream of *wnt11f2* signaling during ANC morphogenesis, where loss of *dact1/2* function recapitulates a loss of *wnt11f2* signaling.

Lineage tracing of *dact1/2* mutant NCC movements reveals their ANC composition

The EP forms from the convergence of a central frontal prominence-derived structure with bilateral maxillary prominence-derived elements (Wada, Javidan et al. 2005, Swartz, Sheehan-Rooney et al. 2011, Dougherty, Kamel et al. 2012, Mork and Crump 2015, Rochard, Monica et al. 2016).The stereotypic convergent migration of cranial neural crest cells and their derivatives presents an excellent model to examine CE movements and their effects on tissue morphogenesis. The zebrafish EP is formed from the joining of a midline frontal prominence derived from the anteromost cranial neural crest (NCC) cell population that migrate over the eyes and turn caudally, to join paired lateral maxillary prominences derived from the second stream of cranial NCC population that migrate rostrally (Kimmel, Miller et al. 2001, Wada, Javidan et al. 2005, Schilling and Le Pabic 2009, Dougherty, Kamel et al. 2012, Mork and Crump 2015). The EP that forms is a planar fan-shaped structure where we and others have shown that the morphology is governed by Wnt signaling (Kimmel, Miller et al. 2001, Rochard, Monica et al. 2016).

Given the rod-like EP we observed in the *dact1-/-; dact2-/-* double mutants, we hypothesized that the dysmorphology could be due to aberrant migration of the anteromost midline stream of cranial NCCs resulting in fusion of the lateral maxillary components. Conversely, an abrogated contribution from the second paired stream of maxillary NCCs could lead to an EP composed entirely of the medial component. To distinguish between these possibilities, we carried out lineage tracing

of the cranial NCC populations in wildtype and *dact1/2* mutants. The *dact1/2* compound mutants were bred onto a *sox10:kaede* transgenic background, where we and others have shown that the *sox10* reporter is a reliable driver of cranial neural crest labeling (Wada, Javidan et al. 2005, Dutton, Antonellis et al. 2008, Swartz, Sheehan-Rooney et al. 2011, Dougherty, Kamel et al. 2012, Kague, Gallagher et al. 2012, Mork and Crump 2015). Cranial NCC populations in wildtype and *dact1/2* mutants were targeted at 19 hpf to photoconvert Kaede reporter protein in either the anterior cranial NCCs that contribute to the frontal prominence, or the second stream of NCCs that contribute to the maxillary prominence, where the labeled cells were followed longitudinally over 4.5 days of development (Fig. 4). We found that the anterior NCCs of wildtype embryos migrated antero-dorsally to the eye and populated the medial EP. To our surprise, the anterior cranial NCC also migrated to contribute to the median element of the rod-like EP, suggesting the complex anterior then caudal migration of the anterior NCC is not disrupted by *dact1/2* mutation (Fig. 4A, arrows). This finding is in contrast to lineage tracing in another midline mutant with a similarly shaped rod-like EP, the *syu* (*sonic hedgehog* null) mutant, where the anterior NCCs failed to populate the ANC (Wada, Javidan et al. 2005).

Next, the second stream of NCC population that contribute to the maxillary prominence was labeled, where they migrate and contribute to the lateral element of the EP as expected in the wildtype (Fig 4B). When the second stream of cranial NCC were labeled and followed in the *dact1/2* mutants, the cells were found to migrate normally up to 36 hpf, but did not ultimately populate the EP in the mutant (arrows), suggesting that the morphological movements after NCC migration were disrupted by loss of *dact1/2*

function. These results suggest that NCC migration itself is not regulated by *dact1/2* but that loss of *dact1/2* hinders the second stream of NCCs' ability to populate the ANC. These results show that the rod-like EP can be formed from 2 different NCC origins, where in the *dact1/2* mutants the EP is contributed by the anteromost frontonasal NCCs, in contrast to the similar rod-shaped EP of the *syu* mutants that is formed from the more posterior stream of maxillary NCCs (Wada, Javidan et al. 2005).

Genetic interaction of *dact1/2* with *gpc4* and *wls* to determine facial morphology

Given the role of Dact/dapper as modifiers of Wnt signaling, we hypothesized that genetic interaction of *dact1/2* with *wls* and *gpc4* will modify facial morphology. Gpc4 is a glycoprotein that binds Wnt ligands and modulates Wnt signaling. *gpc4* zebrafish mutants (*kny*) have impaired CE which leads to a shortened body axis (Topczewski, Sepich et al. 2001). Wls is a posttranslational modifier of Wnt ligands which promotes their secretion (Banziger, Soldini et al. 2006, Bartscherer, Pelte et al. 2006). We previously described that these components of the Wnt/PCP pathway (*gpc4* receptor, *wls* intracellular ligand chaperon, and Wnt ligands *wnt9a* and *wnt5b)* are required for craniofacial morphogenesis, where each gene affects particular morphologic aspects of chondrocytes arrangement in the cardinal axis of the ANC and Meckel's cartilage (Rochard, Monica et al. 2016, Ling, Rochard et al. 2017). Using the EP as a morphologic readout, we examined the genetic interaction of *dact1* and *dact2* with *wls* and *gpc4*. Compound mutants of *dact1*, *dact2, gpc4* or *wls* were generated by breeding the single alleles. Compared to wildtype ANC morphology, abrogation of *gpc4* led to increased width in the transverse axis, but shorter in the antero-posterior axis (Rochard,

Monica et al. 2016). Disruption of *wls* leads to ANC morphology that is also wider in the transverse dimension, but to a lesser degree than observed in *gpc4*. Additionally, in the *wls* mutant, chondrocytes stack in greater layers in the sagittal axis (Rochard, Monica et al. 2016).

Disruption of *gpc4* or *wls* in addition to *dact1/2* generated EP morphology that contained phenotypic attributes from each single mutant, so that the resultant ANC morphology represented a novel ANC form. The EP of a triple homozygous *dact1-/-; dact2-/-; gpc4-/-* mutant was triangular, wider in the transverse axis and shorter in the antero-posterior axis compared to the rod-like ANC observed in the *dact1-/-;dact2-/-* double mutant (Fig. 5A,B). Similarly, the ANC of a triple homozygous *dact1-/-; dact2-/-; wls-/-* mutant was in the shape of a rod, shorter in the antero-posterior axis and thicker in the sagittal axis compared to the *dact1-/-;dact2-/-* double mutant, reflecting attributes of the *wls* mutant (Fig. 5C,D). In addition to the EP phenotypes, the triple homozygous *dact1-/-; dact2-/-; gpc4-/-* mutant also had a short body axis and truncated tail similar but more severe than the *gpc4* mutant (Fig. 5A). Since compound disruption of *dact1*, *dact2*, and *gpc4* or *wls* resulted in a new phenotype we conclude that these genes function in different components of Wnt signaling during craniofacial development.

As we analyzed the subsequent genotypes of our *dact1/dact2/gpc4* triple heterozygote in-cross we gleaned more functional information about *dact1* and *dact2.* We found that *dact1* heterozygosity in the context of *dact2-/-; gpc4-/-* was sufficient to replicate the triple *dact1/dact2/gpc4* homozygous phenotype (Fig. 5E). In contrast, *dact2* heterozygosity in the context of *dact1-/-; gpc4-/-* double mutant produced ANC in the opposite phenotypic spectrum of ANC morphology, appearing similar to the *gpc4-/-*

mutant phenotype (Fig. 5E). These results show that *dact1* and *dact2* do not have redundant function during craniofacial morphogenesis, and that *dact2* function is more indispensable than *dact1*. These results also suggest that *dact1* and *gpc4* may have overlapping roles in craniofacial development.

dact1/2 and _gpc4_ regulate axis extension via overlapping and distinct cellular pathways

Our analyses of axis extension and the hallmarks of a CE defect (namely decreased length and increased width between early tissues) demonstrate that *dact1* and/or *dact2* are required for CE and anterior-posterior axis lengthening during gastrulation (Fig. 3). An axis lengthening and CE defect has also been described in *gpc4* (aka kny) mutants (Topczewski, Sepich et al. 2001). We also observe a defect in axis lengthening in *gpc4-/-* in our hands (representative image Fig. 6A) that is grossly similar to the *dact1/2-/-* mutants. Interestingly, the midfacial hypoplasia of the *wnt11f2* (slb) mutant has been attributed to a defect in axis extension and anterior neural plate patterning (Heisenberg and Nusslein-Volhard 1997), whereas defective axis extension does not lead to midfacial hypoplasia in the *gpc4-/-* mutant. Therefore, we hypothesized that by comparing and contrasting the gene expression changes in *dact1/2* versus *gpc4* mutants during axis extension we could identify cell programs specifically responsible for the anterior axis defect and subsequent midfacial hypoplasia. We performed single-cell transcriptional analysis to compare *dact1/2* mutants, *gpc4* mutants, and wildtype embryos during the segmentation stage. Single-cell encapsulation and barcoded cDNA libraries were prepared from individual dissociated 4 ss wildtype, *dact1-/-;dact2-/-*

compound mutant and *gpc4-/-* mutant embryos using the 10X Genomics Chromium platform and Illumina next-generation sequencing. Genotyping of the embryos was not possible but quality control analysis by considering the top 2000 most variable genes across the dataset showed good clustering by genotype, indicating the reproducibility of individuals in each group. Twenty clusters were identified using Louvain clustering and identity was assigned by reviewing cluster-specific markers in light of published expression data (Farrell, Wang et al. 2018, Farnsworth, Saunders et al. 2020, Bradford, Van Slyke et al. 2022) (Fig. 6B,C). Qualitatively, we did not observe any significant difference in cluster abundance between genotype groups (Fig. S4). We found that *dact1*, *dact2*, and *gpc4* were detected at various levels across clusters, though *dact1* expression was lower than *dact2* (Fig. 6D), consistent with what we observed in RNA wholemount ISH analysis (Fig. 1).

To assess the relative differences in gene expression between genotype groups, we merged clusters into broader cell lineages: ectoderm, axial mesoderm, and paraxial mesoderm (Fig. 7A). We focused on these cell types because they contribute significantly to CE processes and axis establishment. For each of these cell lineages, we performed independent pseudo-bulk differential expression analyses (DEA) of wildtype vs. *dact1-/-;dact2-/-* mutant and wildtype vs. *gpc4-/-* mutant (Fig. 7A). In all 3 cases, we found differentially expressed genes (DEGs) that were commonly in *dact1-/-;dact2-/-* and *gpc4-/-* mutant relative to wildtype (Fig. 7B). To address the hypothesis that *dact1* and *dact2* regulate molecular pathways distinct from those regulated by *gpc4* we also identified genes that were differentially expressed only in *dact1/2-/-* mutants or only in *gpc4-/-* mutants (Fig. 7B). Functional analysis of these DEGs found unique

enrichment of intermediate filament genes in *gpc4-/-* whereas *dact1/2-/-* mutants had enrichment for pathways associated with proteolysis (Fig. 7C, S5). Enrichment for pathways associated with calcium-binding were found in both *gpc4-/-* and *dact1/2-/-*, although the specific DEGs were distinct (Fig. S5). We performed functional analyses specifically for genes that were differentially expressed in *dact1-/-;dact2-/-* mutants, but not in *gpc4-/-* mutants, and found enrichment in pathways associated with proteolysis (Fig. 7B) suggesting a novel role for Dact in embryogenesis.

Interrogation of *dact1-/-;dact2-/-* mutant-specific DEGs found that the calcium-dependent cysteine protease *calpain 8* (*capn8*) was significantly overexpressed in *dact1-/-;dact2-/-* mutants in paraxial mesoderm (103 fold), axial mesoderm (33 fold), and in ectoderm (3 fold; Fig. 7A). We also found that loss of *dact1/2* causes significant changes to *capn8* expression pattern (Fig. 8A). Whereas *capn8* gene expression is principally restricted to the epidermis of wildtype embryos, loss of *dact1/2* leads to significant expansion of ectopic *capn8* gene expression in broader cell types such as in mesodermal tissues (Fig. 8A). We corroborated this finding with wholemount RNA ISH for *capn8* expression in wildtype versus *dact1/2-/-* 12 hpf embryos (Fig. 8B). Expression of *smad1* was also found to be decreased uniquely in the ectoderm of *dact1/2-/-* embryos relative to wildtype (Fig. 7A), however this finding was not investigated further,

Capn8 is considered a “classical” calpain, with domain homology similar to *Capn1* and *Capn2* (Macqueen and Wilcox 2014). In adult human and mouse tissue, *Capn8* expression is largely restricted to the gastrointestinal tract (Sorimachi, Ishiura et al. 1993, Macqueen and Wilcox 2014), however embryonic expression in mammals has not been characterized. Proteolytic targets of Capn8 have not been identified, however,

other classical calpains have been implicated in Wnt and cell-cell/ECM signaling (Konze, van Diepen et al. 2014), including in Wnt/Ca^{+2} regulation of CE in Xenopus (Zanardelli, Christodoulou et al. 2013). To determine whether the *dact1-/-;dact2-/-* mutant craniofacial phenotype could be attributed to *capn8* overexpression, we performed injection of *capn8* or *gfp* control mRNA into 1 cell-stage zebrafish embryos. In wildtype zebrafish, exogenous *capn8* mRNA caused the distinct *dact1/2*-/- craniofacial phenotype including a rod-like ANC at a very low frequency (1 in 142 injected embryos). This phenotype was never observed in wildtype larvae, or when wildtype embryos were injected with an equal concentration of *gfp* mRNA (0 in 192 injected embryos) (Fig. 8C). When mRNA was injected into embryos generated from *dact1/2*+/- interbreeding, *capn8* caused a significant increase in the number of larvae with the mutant craniofacial phenotype (Fig. 8D, 0.0% vs. 7.5%). These findings suggest a new contribution of capn8 to embryonic development as well as anterior neural plate patterning and craniofacial development. Further, the regulation of *capn8* by *dact* may be required for normal embryogenesis and craniofacial morphogenesis.

Discussion

In this study, we examined the genetic requirement of *dact1* and *dact2* during early embryogenesis and craniofacial morphogenesis in zebrafish. Wnt signaling is central to the orchestration of embryogenesis and numerous proteins have been identified as modulators of Wnt signaling, including *Dact1* and *Dact2* (Cheyette, Waxman et al. 2002). Several studies across *Xenopus*, zebrafish, and mouse have ascribed roles to *dact1* and *dact2,* including both promoting and antagonizing Wnt

signaling, depending on the developmental context (Cheyette, Waxman et al. 2002, Gloy, Hikasa et al. 2002, Waxman, Hocking et al. 2004, Gao, Wen et al. 2008, Wen, Chiang et al. 2010, Ma, Liu et al. 2015, Lee, Cheong et al. 2018). Here, we show that *dact1* and *dact2* are required for axis extension during gastrulation and show an example of CE defects during gastrulation associated with craniofacial defects. During axis extension, we show that genetic disruption of *dact2,* but not *dact1,* resulted in a significantly shortened axis relative to wildtype. This result is similar to what was previously found using morpholinos to disrupt *dact1* and *dact2* (Waxman, Hocking et al. 2004). Interestingly, genetically disrupted mutants of *dact1* or *dact2* developed to be phenotypically normal whereas *dact1/2* compound mutants displayed a severe dysmorphic craniofacial phenotype. Again, this is largely similar to the previous morpholino study that found disruption of each gene to cause only a slight and occasional dysmorphic cranial phenotype at 24 hpf (Waxman, Hocking et al. 2004). Notably, embryos injected with a mixture of *dact1* and *dact2* morpholino were not characterized after 10 ss, and the singly injected embryos were not characterized after 24 hpf (Waxman, Hocking et al. 2004). Therefore, by analyzing genetic mutants of dact1 and dact2 our findings have largely validated the previous morpholino literature as well as added new data on later developmental outcomes.

The gene expression and genetic epistasis experiments carried out here support that the *dact* paralogs are not redundant and have unique functions during different stages of embryonic and larval development. We observed that *dact1* and *dact2* have distinct spatiotemporal expression patterns throughout embryogenesis, suggesting unique roles for each paralog in developmental processes. Differential expression of

Dact1 and *Dact2* was also described during odontogenesis in mice (Kettunen, Kivimae et al. 2010). This aligns with previous findings of differential roles of *dact1* and *dact2* in canonical vs. non-canonical Wnt signaling (Waxman, Hocking et al. 2004) and a specific role for *dact2*, but not *dact1*, in TGF-beta signaling (Su, Zhang et al. 2007, Schubert, Sobreira et al. 2014). However, the lack of a resultant phenotype upon genetic ablation of *dact1* or *dact2* individually suggests the capability of functional compensation. This is puzzling given their distinct expression patterns and needs to be examined further.

We found that *dact1* and *dact2* contribute to axis extension, and their compound mutants exhibit a shortened and widened body axis that is consistent with a CE defect during gastrulation. This finding aligns with previous studies that have implicated *dact1* and *dact2* in non-canonical Wnt signaling and regulation of embryonic axis extension (Waxman, Hocking et al. 2004). Based on our gene expression and combinatorial genetic analyses, we offer the hypothesis that *dact1* expression in the paraxial mesoderm is required for dorsal CE during gastrulation through its role in noncanonical Wnt/PCP signaling, similar to the defect observed upon *gpc4* disruption. Conversely, we posit that *dact2* functions in the prechordal mesoderm to promote anterior migration during gastrulation, a function which has also been ascribed to *wntllf2* (Heisenberg and Nusslein-Volhard 1997). It is only upon loss of both *dact1* and *dact2* functions that the axis is significantly truncated and a craniofacial malformation results. Further experiments with spatially restricted gene ablation or cell transplantation are required to test this hypothesis.

Our results underscore the crucial roles of *dact1* and *dact2* in embryonic development and suggest a connection between gastrulation movements and

subsequent craniofacial morphogenesis. Our finding that in *dact1-/-;dact2-/-* compound mutants the first stream of CNCC migrate and contribute to the ANC, while the second stream fails to contribute suggests the possibility of an anatomical barrier to migration, rather than an autonomous defect of the CNCCs. Disruption of the sonic hedgehog signaling pathway in zebrafish results in a similar phenotype to *dact1-/-;dact2-/-* and *wntllf2-/-* mutants where the eyes converge medially and the EP narrows to a rod shape. Interestingly, lineage tracing analysis in hedgehog-disrupted embryos found the rod-like EP to consist solely of second stream-derived CNCCs (Wada, Javidan et al. 2005). This is in contrast to the *dact1-/-;dact2-/-* mutants, demonstrating two different cellular mechanisms that result in a similar anatomical dysmorphology. It will be important to test the generality of this phenomenon and determine if other mutants with craniofacial abnormalities have early patterning differences. Further, a temporally conditional genetic knockout is needed to definitively test the connection between early and later development.

By comparing the transcriptome across different Wnt genetic contexts, i.e. *gpc4-/-* with that of the *dact1-/-;dact2-/-* compound mutant, we identified a novel role for *dact1/2* in the regulation of proteolysis, with significant misexpression of *capn8* in the mesoderm of *dact1-/-;dact2-/-* mutants. Although at a very low frequency, ectopic expression of *capn8* mRNA recapitulated the *dact1-/-;dact2-/-* mutant craniofacial phenotype, suggesting that inhibition of *capn8* expression in the mesoderm by dact is required for normal morphogenesis. Genes involved in calcium ion binding were also differentially expressed in the *dact1-/-;dact2-/-* mutants and we predict that altering

intracellular calcium handling in conjunction with *capn8* overexpression would increase the frequency of the recapitulated *dact1-/-;dact2-/-* mutant phenotype.

Capn8 is described as a stomach-specific calpain and a role during embryogenesis has not been previously described. Calpains are typically calcium-activated proteases and it is feasible that Capn8 is active in response to Wnt/Ca^{2+} signaling. A close family member, Capn2 has been found to modulate Wnt signaling by degradation of beta-catenin (Zanardelli, Christodoulou et al. 2013, Konze, van Diepen et al. 2014). These findings suggest that dact-dependent suppression of *capn8* expression is necessary for normal embryogenesis and craniofacial morphogenesis, further expanding the functional repertoire of *dact1/2*. Further research is required to examine the direct regulatory role of dacts on *capn8* expression. Our findings also warrant investigation into the role of *capn8* during embryogenesis and possible implications for known craniofacial or other disorders. Recently, Capn8 has been implicated in EMT associated with cancer metastasis (Zhong, Xu et al. 2022, Song, Cui et al. 2024) and Xenopus capn8 was found to be required for CNCC migration (Cousin, Abbruzzese et al. 2011). Together these findings support a role of *capn8* in CNCC migration and craniofacial morphogenesis.

Another gene identified in our scRNA-seq data to be differentially expressed in the *dact1-/-,dact2-/-* but not the *gpc4-/-* embryos was *smad1*. Smad1 acts in the TGF-β signaling pathway and dact2 has been described to inhibit TGF-β and Nodal signaling by promoting the degradation of Nodal receptors (Zhang, Zhou et al. 2004, Su, Zhang et al. 2007, Meng, Cheng et al. 2008, Kivimae, Yang et al. 2011). Zebrafish Nodal pathway mutants (*cyc/ndr2*, *oep/tdgf1*, *sqt/ndr1*) exhibit medially displaced eyes (Hatta, Kimmel

et al. 1991, Brand, Heisenberg et al. 1996, Heisenberg and Nusslein-Volhard 1997, Feldman, Gates et al. 1998, Zhang, Talbot et al. 1998) and it is robustly feasible that dysregulation of TGF- β signaling in the *dact1*-/-;*dact2*-/- mutant contributes to the craniofacial phenotype. Future research will examine the role of *dact1* and *dact2* in the coordination of Wnt and TGF-β signaling and the importance of this coordination in the context of craniofacial development. Of note, Sonic Hedgehog (shh) signaling is a principal regulator to the vertebrate midline (Chiang, Litingtung et al. 1996, Ribes, Balaskas et al. 2010), and important in the development of the zebrafish floorplate (Halpern, Hatta et al. 1997, Odenthal, van Eeden et al. 2000). Mutants with disrupted *shh* expression or signaling (*cyc/ndr2*, *smo, oep/tdgf1*) exhibit medially displaced eyes similar to the *dact1/2* mutants (Brand, Heisenberg et al. 1996, Chen, Burgess et al. 2001). We did not find any genes within the sonic hedgehog pathway to be differentially expressed in *dact1/2* mutants, though post-transcriptional interactions cannot be ruled out.

This study has uncovered the genetic requirement of *dact1* and *dact2* in embryonic CE and craniofacial morphogenesis, delineated the genetic interaction with Wnt genes and identified capn8 as a modifier of this process. As with most studies, this work has contributed some new knowledge but generated more questions than answers. Future work will delineate the molecular differences across the different *dact1/2* and other Wnt mutants to further identify determinants of craniofacial morphogenesis; and to connect these findings to clinically important Wnt regulators of facial morphology and pathology.

Methods

Animals and CRISPR/Cas9 targeted mutagenesis

All animal husbandry and experiments were performed in accordance with approval from Massachusetts General Hospital Institutional Animal Care and Usage Committee. Zebrafish (*Danio rerio*) embryos and adults were maintained in accordance with institutional protocols. Embryos were raised at 28.5 C in E3 medium (Carroll, Macias Trevino et al. 2020) and staged visually and according to standardized developmental timepoints (Westerfield 1993). All zebrafish lines used for experiments and gene editing were generated from the Tubingen or AB strain. The *wnt11f2* mutant line and gpc4-/- mutant line were obtained from Zebrafish International Resource Center (wnt11f2$^{tx226/+}$ and gpc4$^{hi1688Tg/+}$ respectively). The *wls*-/- mutant line was originally gifted to the lab and independently generated, as previously described (Rochard, Monica et al. 2016). The *sox10*:kaede transgenic line was previously generated and described by our lab (Dougherty, Kamel et al. 2012).

CRISPR sgRNA guides were designed using computational programs ZiFiT Targeter v4.2 (zifit.partners.org/ZiFit) (Sander, Zaback et al. 2007), crispr.mit.edu (https://zlab.bio/guide-design-resouces) (Ran, Hsu et al. 2013), and ChopChop (https://chopchop.cbu.uib.no) (Montague, Cruz et al. 2014) with traditional sequence constraints. Guides were chosen that were predicted to give high efficiency and specificity. Guides best meeting these parameters were selected in exon 2 of *dact1* and exon 4 of *dact2*. No suitable gRNA with sufficient efficiency were identified for *dact2* 5'

of exon 4 and the resulting phenotype was reassuring compared to previous morpholino published results. Guides for *dact1* and *dact2* and Cas9 protein were prepared and microinjected into 1 cell-stage zebrafish embryos and founders were identified as previously described (Carroll, Macias Trevino et al. 2020). Primers flanking the sgRNA guide site were designed for genotyping and fragment analysis was performed on genomic DNA to detect base pair insertion/deletion. Sanger sequencing was performed to verify targeted gene mutation and confirm the inclusion of a premature stop codon. *dact1* forward primer: TACAGAAGCTGCTGAAGTACCG, *dact1* reverse primer: CCCTCTCTCAAAGTGTTTTGGT, *dact2* forward primer: TGAAGAGCTCCACTCCCCTGT, *dact2* reverse primer: GCAGTTGAGGTCCATTCAGC.

RT qPCR analysis

Pooled wildtype, *dact1*-/-, *dact2*-/-, and *dact1/2*-/- fish were collected and RNA extractions were performed using RNeasy Mini Kit (Qiagen). cDNA was generated using High Capacity cDNA Reverse Transcription Kit (ThermoFisher). Quantitative PCR (qPCR) was performed using *dact1* (Dr03152516_m1) and *dact2* (Dr03426298_s1) TaqMan Gene Expression Assays. Expression was normalized to 18S rRNA expression (Hs03003631_g1). TaQman Fast Advanced master mix (ThermoFisher) and a StepOnePlus Real-Time PCR system (Applied Biosystems) were used to measure relative mRNA levels, which were calculated using the ddCT method.

Microinjection of mRNA

Template DNA for *in vivo* mRNA transcription was generated by PCR amplification of the gene of interest from a zebrafish embryo cDNA library and cloning into pCS2+8 destination plasmid. mRNA for injection was generated using an *in vitro* transcription kit (Invitrogen mMessage mMachine). One-cell stage zebrafish embryos were injected with 2 nL of mRNA in solution. To test genetic knockout specificity, 150 or 300 pg or dact1, dact2 or dact1 and dact2 mRNA was injected. For capn8 overexpression analysis 200 pg or GFP or capn8 mRNA was injected. Following phenotyping analysis, genotypes were determined by fragment analysis of *dact1* and *dact2* genotyping PCR products.

Wholemount and RNAscope *in situ* hybridization

Wholemount *in situ* hybridization was performed as previously described (Carroll, Macias Trevino et al. 2020). Zebrafish embryonic cDNA was used as a template to generate riboprobes. Primers were designed to PCR amplify the specific riboprobe sequence with a T7 promoter sequence linked to the reverse primer. *In vitro* transcription was performed using a T7 polymerase and DIG-labeled nucleotides (Roche). RNAscope was performed on sectioned zebrafish larvae as previously described (Carroll, Macias Trevino et al. 2020). Probes were designed by and purchased from ACD Bio. Hybridization and detection was performed according to the manufacturer's protocol. Sections were imaged using a confocal microscope (Leica SP8) and z-stack maximum projections were generated using Fiji software.

Alcian blue staining and imaging

Alcian blue staining and imaging were performed at 4 dpf as previously described (Carroll, Macias Trevino et al. 2020). Briefly, larvae were fixed in 4% v/v formaldehyde overnight at 4°C. Larvae were dehydrated in 50% v/v ethanol and stained with Alcian blue as described (Walker and Kimmel 2007). Whole and dissected larvae were imaged in 3% w/v methylcellulose using a Nikon Eclipse 80i compound microscope with a Nikon DS Ri1 camera. Z-stacked images were taken and extended depth of field was calculated using NIS Element BR 3.2 software. Images were processed using Fiji software. After image capture embryos were genotyped by PCR and fragment analysis.

Axis measurements

Compound *dact1+/-*; *dact2+/-* zebrafish were in-crossed and progeny were collected from 2 separate clutches and fixed in 4% formaldehyde at approximately 8ss. Embryos were individually imaged using a Zeiss Axiozoom stereoscope and processed for DNA extraction and genotyping (Westerfield 1993). Images were analyzed using Fiji. A circle was drawn to overlay the yolk and the geometric center was determined using the function on Fiji. Using the Fiji angle tool, lines were drawn from the center point to the anterior-most point of the embryo and from the center to the posterior-most point of the embryo. The resulting inner angle of these lines was determined. Each angle measurement was then calculated as a ratio to the average angle of the wildtype embryos. ANOVA was performed to determine statistical significance, $p<0.05$.

Lineage analysis of CNCCs

Live embryos were mounted in 1% w/v low melt agarose and covered with E3 medium containing 0.013% w/v tricaine. Wildtype control and dact1/2-/- compound mutants on a Tg(*soxl0*:kaede) background were imaged on a Leica DMi8 confocal microscope and photoconverted using the UV laser (404 nm) until the green kaede fluorescence disappeared. For each embryo, one side was photoconverted and the contralateral side served as an internal control. After photoconversion, embryos were removed from the agarose and raised in E3 medium at 28.5 C until the required developmental timepoint, at which time they were similarly re-mounted and re-imaged. Z-stacked images were processed as maximum-intensity projections using Fiji software.

Single-cell RNA sequencing (scRNA-seq)

Single-cell transcriptomic analyses were performed on 10 zebrafish embryos, including 4 wildtype, 3 *dact1-/-;dact2-/-* compound mutant, and 3 *gpc4-/-* mutant embryos. Embryos were collected at 4 ss with *dact1-/-,dact2-/-* and *gpc4-/-* mutants being identified by their truncated body axis. Embryos were dechorionated with a short (approximately 10 min) incubation in 1 mg/ml Pronase and then washed 3x in embryo medium. Cell dissociation was performed with modifications as previously described (Farrell, Wang et al. 2018). Each embryo was transferred to 50 μl DMEM/F12 media on ice. To dissociate cells, media was replaced with 200 μl DPBS (without Ca^{2+} and Mg^{2+}) with 0.1% w/v BSA. Embryos were disrupted by pipetting 10x with a P200 pipette tip. 500 μl of DPBS + 0.1% BSA was added and cells were centrifuged at 300xg for 1 min. Cell pellets were resuspended in 200 μl DPBS + 0.1% BSA and kept on ice. Just prior to encapsulation, cells were passed through a 40 μm cell strainer, and cell counts and

viability were measured. After droplet encapsulation, barcoding, and library preparation using the 10X Genomics Chromium Single Cell 3' kit (version 3), data were sequenced on an Illumina NovaSeq 6000 sequencer.

FASTQ files were demultiplexed and aligned to the GRCz11 build of the zebrafish genome using Cellranger (version 6.1.0) (Zheng, Terry et al. 2017). Raw Cellranger count matrices were imported into R (version 4.1.2) using Seurat (version 4.1.0) (Hao, Hao et al. 2021). First, we reviewed data for quality and excluded any droplet that did not meet all of the following criteria: (i) have at least 1,500 unique molecular identifiers (UMIs), (ii) covering at least 750 distinct genes; (iii) have <5% of genes mapping to the mitochondrial genome; and (iv) have a log10 of detected genes per UMI >80%. After quality control, the dataset was also filtered to exclude genes with a detection rate below 1 in 3,000 cells, leaving a total of 20,078 distinct genes expressed across 19,457 cells for analysis.

The quality-controlled count data were normalized using Pearson's residuals from the regularized negative binomial regression model, as implemented in Seurat::SCTransfrom (Hafemeister and Satija 2019). When computing the SCT model, the effect of the total number of UMIs and number of detected genes per cell were regressed out. After normalization, the top 3,000 most variably expressed genes were used to calculate principal components (PCs). Data were then integrated by source sample using Harmony (version 0.1.0) (Korsunsky, Millard et al. 2019). A two-dimensional uniform manifold approximation and projection (UMAP) (Becht, McInnes et al. 2018) was then derived from the first 40 Harmony embeddings for visualization.

Using the integrated Harmony embeddings, clusters were defined with the Louvain clustering method, as implemented within Seurat. A resolution of 0.3 was used for cluster definition. Cluster identities were assigned by manually reviewing the results of Seurat::FindAllMarkers, searching for genes associated to known developmental lineages. Gene expression data for key markers that guided cluster identity assignment were visualized using Seurat::DotPlot.

Following this detailed annotation, some clusters were grouped to focus downstream analyses on 3 major lineages: ventral mesoderm (grouping cells from the pronephros, vasculogenic/myeloid precursors, hematopoietic cells, heart primordium, and cephalic mesoderm clusters), dorsal mesoderm (adaxial cells, segmental plate, and paraxial mesoderm), ectoderm (CNS, mid/hindbrain boundary, spinal cord, and neural crest). For those 3 lineages, single-cell level data were aggregated per sample and cluster to perform pseudobulk differential expression analyses (DEA) contrasting genotypes. Independent pairwise comparisons of *dact1-/-;dact2-/-* versus wildtype and *gpc4-/-* vs wildtype were performed using DESeq2 (v1.34.0) (Love, Huber et al. 2014). P-values were corrected for multiple testing using the default Benjamini-Hochberg method; log2 fold change values were corrected using the apeglm shrinkage estimator (Zhu, Ibrahim et al. 2019). Significance was defined as an adjusted p-value < 0.1 and log2 fold change > 0.58 in absolute value. Heatmaps of the top most significant differentially expressed genes were generated from the regularized log transformed data using pheatmap (version 1.0.12). Overlap in significant genes across pairwise comparisons were determined and visualized in Venn diagrams. Over-representation analyses against the Gene Ontology (GO) database were ran using clusterProfiler

(version 4.2.2) (Wu, Hu et al. 2021), using as input the set of genes found to be differentially expressed in the comparison of *dact1-/-;dact-/-* versus wildtype but not *gpc4-/-* versus wildtype. Sequencing data have been deposited in GEO under accession code GSE240264.

Statistical analysis

Analyses were performed using Prism Software (GraphPad) unless otherwise specified. An unpaired Student's *t* test or one-way ANOVA with multiple comparisons was used as indicated and a *P*-value <0.05 was considered significant. Graphs represent the mean +/- the SEM and *n* represents biological replicates. For categorical data (normal vs. mutant phenotype) a Fisher exact test was performed between *gfp* and *capn8* injected embryos and the odds ratio was determined. The confidence interval was determined by the Baptista-Pike method.

Acknowledgments

We thank Christoph Seiler, Adele Donohue and the Aqautics Facility team at Children's Hospital of Philadelphia; and Jessica Bethoney at Massachusetts General Hospital (MGH) for their excellent management of our zebrafish colonies and facilities. We thank the MGH Next Generation Sequencing Core for cell encapsulation, cDNA library preparation, and sequencing. Single-cell sequencing analysis was performed by the Harvard Chan Bioinformatics Core. Work by A.J. was funded in part by the Harvard Stem Cell Institute. We appreciate and acknowledge the generous funding support from

the Shriners Hospitals for Children. This work was supported by the National Institutes of Health grant R01DE027983 to E.C.L.

References

Alhazmi, N., S. H. Carroll, K. Kawasaki, K. C. Woronowicz, S. A. Hallett, C. Macias Trevino, E. B. Li, R. Baron, F. Gori, P. C. Yelick, M. P. Harris and E. C. Liao (2021). "Synergistic roles of Wnt modulators R-spondin2 and R-spondin3 in craniofacial morphogenesis and dental development." Sci Rep **11**(1): 5871.

Banziger, C., D. Soldini, C. Schutt, P. Zipperlen, G. Hausmann and K. Basler (2006). "Wntless, a conserved membrane protein dedicated to the secretion of Wnt proteins from signaling cells." Cell **125**(3): 509-522.

Bartscherer, K., N. Pelte, D. Ingelfinger and M. Boutros (2006). "Secretion of Wnt ligands requires Evi, a conserved transmembrane protein." Cell **125**(3): 523-533.

Becht, E., L. McInnes, J. Healy, C. A. Dutertre, I. W. H. Kwok, L. G. Ng, F. Ginhoux and E. W. Newell (2018). "Dimensionality reduction for visualizing single-cell data using UMAP." Nat Biotechnol.

Bradford, Y. M., C. E. Van Slyke, L. Ruzicka, A. Singer, A. Eagle, D. Fashena, D. G. Howe, K. Frazer, R. Martin, H. Paddock, C. Pich, S. Ramachandran and M. Westerfield (2022). "Zebrafish information network, the knowledgebase for Danio rerio research." Genetics **220**(4).

Brand, M., C. P. Heisenberg, R. M. Warga, F. Pelegri, R. O. Karlstrom, D. Beuchle, A. Picker, Y. J. Jiang, M. Furutani-Seiki, F. J. van Eeden, M. Granato, P. Haffter, M. Hammerschmidt, D. A. Kane, R. N. Kelsh, M. C. Mullins, J. Odenthal and C. Nusslein-Volhard (1996). "Mutations affecting development of the midline and general body shape during zebrafish embryogenesis." Development **123**: 129-142.

Brott, B. K. and S. Y. Sokol (2005). "Frodo proteins: modulators of Wnt signaling in vertebrate development." Differentiation **73**(7): 323-329.

Carroll, S. H., C. Macias Trevino, E. B. Li, K. Kawasaki, N. Myers, S. A. Hallett, N. Alhazmi, J. Cotney, R. P. Carstens and E. C. Liao (2020). "An Irf6-Esrp1/2 regulatory axis controls midface morphogenesis in vertebrates." Development **147**(24).

Chen, W., S. Burgess and N. Hopkins (2001). "Analysis of the zebrafish smoothened mutant reveals conserved and divergent functions of hedgehog activity." Development **128**(12): 2385-2396.

Cheyette, B. N., J. S. Waxman, J. R. Miller, K. Takemaru, L. C. Sheldahl, N. Khlebtsova, E. P. Fox, T. Earnest and R. T. Moon (2002). "Dapper, a Dishevelled-associated antagonist of beta-catenin and JNK signaling, is required for notochord formation." Dev Cell **2**(4): 449-461.

Chiang, C., Y. Litingtung, E. Lee, K. E. Young, J. L. Corden, H. Westphal and P. A. Beachy (1996). "Cyclopia and defective axial patterning in mice lacking Sonic hedgehog gene function." Nature **383**(6599): 407-413.

828 Clevers, H. and R. Nusse (2012). "Wnt/beta-catenin signaling and disease." Cell **149**(6): 1192-
829 1205.

830 Corey, D. R. and J. M. Abrams (2001). "Morpholino antisense oligonucleotides: tools for
831 investigating vertebrate development." Genome Biol **2**(5): REVIEWS1015.

832 Cousin, H., G. Abbruzzese, E. Kerdavid, A. Gaultier and D. Alfandari (2011). "Translocation of the
833 cytoplasmic domain of ADAM13 to the nucleus is essential for Calpain8-a expression and cranial
834 neural crest cell migration." Dev Cell **20**(2): 256-263.

835 Dougherty, M., G. Kamel, V. Shubinets, G. Hickey, M. Grimaldi and E. C. Liao (2012). "Embryonic
836 fate map of first pharyngeal arch structures in the sox10: kaede zebrafish transgenic model." J
837 Craniofac Surg **23**(5): 1333-1337.

838 Dutton, J. R., A. Antonellis, T. J. Carney, F. S. Rodrigues, W. J. Pavan, A. Ward and R. N. Kelsh
839 (2008). "An evolutionarily conserved intronic region controls the spatiotemporal expression of
840 the transcription factor Sox10." BMC Dev Biol **8**: 105.

841 Farnsworth, D. R., L. M. Saunders and A. C. Miller (2020). "A single-cell transcriptome atlas for
842 zebrafish development." Dev Biol **459**(2): 100-108.

843 Farrell, J. A., Y. Wang, S. J. Riesenfeld, K. Shekhar, A. Regev and A. F. Schier (2018). "Single-cell
844 reconstruction of developmental trajectories during zebrafish embryogenesis." Science
845 **360**(6392).

846 Feldman, B., M. A. Gates, E. S. Egan, S. T. Dougan, G. Rennebeck, H. I. Sirotkin, A. F. Schier and
847 W. S. Talbot (1998). "Zebrafish organizer development and germ-layer formation require nodal-
848 related signals." Nature **395**(6698): 181-185.

849 Gao, X., J. Wen, L. Zhang, X. Li, Y. Ning, A. Meng and Y. G. Chen (2008). "Dapper1 is a
850 nucleocytoplasmic shuttling protein that negatively modulates Wnt signaling in the nucleus." J
851 Biol Chem **283**(51): 35679-35688.

852 Gillhouse, M., M. Wagner Nyholm, H. Hikasa, S. Y. Sokol and Y. Grinblat (2004). "Two
853 Frodo/Dapper homologs are expressed in the developing brain and mesoderm of zebrafish."
854 Dev Dyn **230**(3): 403-409.

855 Gloy, J., H. Hikasa and S. Y. Sokol (2002). "Frodo interacts with Dishevelled to transduce Wnt
856 signals." Nat Cell Biol **4**(5): 351-357.

857 Hafemeister, C. and R. Satija (2019). "Normalization and variance stabilization of single-cell
858 RNA-seq data using regularized negative binomial regression." Genome Biol **20**(1): 296.

859 Halpern, M. E., K. Hatta, S. L. Amacher, W. S. Talbot, Y. L. Yan, B. Thisse, C. Thisse, J. H.
860 Postlethwait and C. B. Kimmel (1997). "Genetic interactions in zebrafish midline development."
861 Dev Biol **187**(2): 154-170.

862 Hammerschmidt, M., F. Pelegri, M. C. Mullins, D. A. Kane, M. Brand, F. J. van Eeden, M.
863 Furutani-Seiki, M. Granato, P. Haffter, C. P. Heisenberg, Y. J. Jiang, R. N. Kelsh, J. Odenthal, R. M.
864 Warga and C. Nusslein-Volhard (1996). "Mutations affecting morphogenesis during gastrulation
865 and tail formation in the zebrafish, Danio rerio." Development **123**: 143-151.

866 Hao, Y., S. Hao, E. Andersen-Nissen, W. M. Mauck, 3rd, S. Zheng, A. Butler, M. J. Lee, A. J. Wilk,
867 C. Darby, M. Zager, P. Hoffman, M. Stoeckius, E. Papalexi, E. P. Mimitou, J. Jain, A. Srivastava, T.
868 Stuart, L. M. Fleming, B. Yeung, A. J. Rogers, J. M. McElrath, C. A. Blish, R. Gottardo, P. Smibert
869 and R. Satija (2021). "Integrated analysis of multimodal single-cell data." Cell **184**(13): 3573-
870 3587 e3529.

871 Hashimoto, M., H. Morita and N. Ueno (2014). "Molecular and cellular mechanisms of
872 development underlying congenital diseases." Congenit Anom (Kyoto) **54**(1): 1-7.

873 Hatta, K., C. B. Kimmel, R. K. Ho and C. Walker (1991). "The cyclops mutation blocks
874 specification of the floor plate of the zebrafish central nervous system." Nature **350**(6316): 339-
875 341.

876 Heasman, J. (2002). "Morpholino oligos: making sense of antisense?" Dev Biol **243**(2): 209-214.

877 Heisenberg, C. P., M. Brand, Y. J. Jiang, R. M. Warga, D. Beuchle, F. J. van Eeden, M. Furutani-
878 Seiki, M. Granato, P. Haffter, M. Hammerschmidt, D. A. Kane, R. N. Kelsh, M. C. Mullins, J.
879 Odenthal and C. Nusslein-Volhard (1996). "Genes involved in forebrain development in the
880 zebrafish, Danio rerio." Development **123**: 191-203.

881 Heisenberg, C. P. and C. Nusslein-Volhard (1997). "The function of silberblick in the positioning
882 of the eye anlage in the zebrafish embryo." Dev Biol **184**(1): 85-94.

883 Heisenberg, C. P., M. Tada, G. J. Rauch, L. Saude, M. L. Concha, R. Geisler, D. L. Stemple, J. C.
884 Smith and S. W. Wilson (2000). "Silberblick/Wnt11 mediates convergent extension movements
885 during zebrafish gastrulation." Nature **405**(6782): 76-81.

886 Hikasa, H. and S. Y. Sokol (2004). "The involvement of Frodo in TCF-dependent signaling and
887 neural tissue development." Development **131**(19): 4725-4734.

888 Hunter, N. L., H. Hikasa, S. M. Dymecki and S. Y. Sokol (2006). "Vertebrate homologues of Frodo
889 are dynamically expressed during embryonic development in tissues undergoing extensive
890 morphogenetic movements." Dev Dyn **235**(1): 279-284.

891 Huybrechts, Y., G. Mortier, E. Boudin and W. Van Hul (2020). "WNT Signaling and Bone: Lessons
892 From Skeletal Dysplasias and Disorders." Front Endocrinol (Lausanne) **11**: 165.

893 Ji, Y., H. Hao, K. Reynolds, M. McMahon and C. J. Zhou (2019). "Wnt Signaling in Neural Crest
894 Ontogenesis and Oncogenesis." Cells **8**(10).

895 Kague, E., M. Gallagher, S. Burke, M. Parsons, T. Franz-Odendaal and S. Fisher (2012).
896 "Skeletogenic fate of zebrafish cranial and trunk neural crest." PLoS One **7**(11): e47394.

897 Kamel, G., T. Hoyos, L. Rochard, M. Dougherty, Y. Kong, W. Tse, V. Shubinets, M. Grimaldi and E.
898 C. Liao (2013). "Requirement for frzb and fzd7a in cranial neural crest convergence and
899 extension mechanisms during zebrafish palate and jaw morphogenesis." Dev Biol **381**(2): 423-
900 433.

901 Kettunen, P., S. Kivimae, P. Keshari, O. D. Klein, B. N. Cheyette and K. Luukko (2010). "Dact1-3
902 mRNAs exhibit distinct expression domains during tooth development." Gene Expr Patterns
903 **10**(2-3): 140-143.

904 Kim, D. H., E. J. Kim, D. H. Kim and S. W. Park (2020). "Dact2 is involved in the regulation of
905 epithelial-mesenchymal transition." Biochem Biophys Res Commun **524**(1): 190-197.

906 Kimmel, C. B., C. T. Miller and C. B. Moens (2001). "Specification and morphogenesis of the
907 zebrafish larval head skeleton." Dev Biol **233**(2): 239-257.

908 Kivimae, S., X. Y. Yang and B. N. Cheyette (2011). "All Dact (Dapper/Frodo) scaffold proteins
909 dimerize and exhibit conserved interactions with Vangl, Dvl, and serine/threonine kinases."
910 BMC Biochem **12**: 33.

911 Kok, F. O., M. Shin, C. W. Ni, A. Gupta, A. S. Grosse, A. van Impel, B. C. Kirchmaier, J. Peterson-
912 Maduro, G. Kourkoulis, I. Male, D. F. DeSantis, S. Sheppard-Tindell, L. Ebarasi, C. Betsholtz, S.
913 Schulte-Merker, S. A. Wolfe and N. D. Lawson (2015). "Reverse genetic screening reveals poor
914 correlation between morpholino-induced and mutant phenotypes in zebrafish." Dev Cell **32**(1):
915 97-108.

916 Konze, S. A., L. van Diepen, A. Schroder, R. Olmer, H. Moller, A. Pich, R. Weissmann, A. W. Kuss,
917 R. Zweigerdt and F. F. Buettner (2014). "Cleavage of E-cadherin and beta-catenin by calpain
918 affects Wnt signaling and spheroid formation in suspension cultures of human pluripotent stem
919 cells." Mol Cell Proteomics **13**(4): 990-1007.

920 Korsunsky, I., N. Millard, J. Fan, K. Slowikowski, F. Zhang, K. Wei, Y. Baglaenko, M. Brenner, P. R.
921 Loh and S. Raychaudhuri (2019). "Fast, sensitive and accurate integration of single-cell data
922 with Harmony." Nat Methods **16**(12): 1289-1296.

923 Lee, H., S. M. Cheong, W. Han, Y. Koo, S. B. Jo, G. S. Cho, J. S. Yang, S. Kim and J. K. Han (2018).
924 "Head formation requires Dishevelled degradation that is mediated by March2 in concert with
925 Dapper1." Development **145**(7).

926 Li, X., S. Florez, J. Wang, H. Cao and B. A. Amendt (2013). "Dact2 represses PITX2 transcriptional
927 activation and cell proliferation through Wnt/beta-catenin signaling during odontogenesis."
928 PLoS One **8**(1): e54868.

929 Ling, I. T., L. Rochard and E. C. Liao (2017). "Distinct requirements of wls, wnt9a, wnt5b and
930 gpc4 in regulating chondrocyte maturation and timing of endochondral ossification." Dev Biol
931 **421**(2): 219-232.

932 Logan, C. Y. and R. Nusse (2004). "The Wnt signaling pathway in development and disease."
933 Annu Rev Cell Dev Biol **20**: 781-810.

934 Loh, K. M., R. van Amerongen and R. Nusse (2016). "Generating Cellular Diversity and Spatial
935 Form: Wnt Signaling and the Evolution of Multicellular Animals." Dev Cell **38**(6): 643-655.

936 Love, M. I., W. Huber and S. Anders (2014). "Moderated estimation of fold change and
937 dispersion for RNA-seq data with DESeq2." Genome Biol **15**(12): 550.

938 Ma, B., B. Liu, W. Cao, C. Gao, Z. Qi, Y. Ning and Y. G. Chen (2015). "The Wnt Signaling
939 Antagonist Dapper1 Accelerates Dishevelled2 Degradation via Promoting Its Ubiquitination and
940 Aggregate-induced Autophagy." J Biol Chem **290**(19): 12346-12354.

941 Macqueen, D. J. and A. H. Wilcox (2014). "Characterization of the definitive classical calpain
942 family of vertebrates using phylogenetic, evolutionary and expression analyses." Open Biol **4**(4):
943 130219.

944 Mehta, S., S. Hingole and V. Chaudhary (2021). "The Emerging Mechanisms of Wnt Secretion
945 and Signaling in Development." Front Cell Dev Biol **9**: 714746.

946 Meng, F., X. Cheng, L. Yang, N. Hou, X. Yang and A. Meng (2008). "Accelerated re-
947 epithelialization in Dpr2-deficient mice is associated with enhanced response to TGFbeta
948 signaling." J Cell Sci **121**(Pt 17): 2904-2912.

949 Montague, T. G., J. M. Cruz, J. A. Gagnon, G. M. Church and E. Valen (2014). "CHOPCHOP: a
950 CRISPR/Cas9 and TALEN web tool for genome editing." Nucleic Acids Res **42**(Web Server issue):
951 W401-407.

952 Morcos, P. A., A. C. Vincent and J. D. Moulton (2015). "Gene Editing Versus Morphants."
953 Zebrafish **12**(5): 319.

954 Mork, L. and G. Crump (2015). "Zebrafish Craniofacial Development: A Window into Early
955 Patterning." Curr Top Dev Biol **115**: 235-269.

956 Muyskens, J. B. and C. B. Kimmel (2007). "Tbx16 cooperates with Wnt11 in assembling the
957 zebrafish organizer." Mech Dev **124**(1): 35-42.

958 Nasevicius, A. and S. C. Ekker (2000). "Effective targeted gene 'knockdown' in zebrafish." Nat
959 Genet **26**(2): 216-220.

960 Niehrs, C. (2012). "The complex world of WNT receptor signalling." Nat Rev Mol Cell Biol **13**(12):
961 767-779.

962 Odenthal, J., F. J. van Eeden, P. Haffter, P. W. Ingham and C. Nusslein-Volhard (2000). "Two
963 distinct cell populations in the floor plate of the zebrafish are induced by different pathways."
964 Dev Biol **219**(2): 350-363.

965 Oteiza, P., M. Koppen, M. Krieg, E. Pulgar, C. Farias, C. Melo, S. Preibisch, D. Muller, M. Tada, S.
966 Hartel, C. P. Heisenberg and M. L. Concha (2010). "Planar cell polarity signalling regulates cell
967 adhesion properties in progenitors of the zebrafish laterality organ." Development **137**(20):
968 3459-3468.

969 Petersen, C. P. and P. W. Reddien (2009). "Wnt signaling and the polarity of the primary body
970 axis." Cell **139**(6): 1056-1068.

971 Piotrowski, T., T. F. Schilling, M. Brand, Y. J. Jiang, C. P. Heisenberg, D. Beuchle, H. Grandel, F. J.
972 van Eeden, M. Furutani-Seiki, M. Granato, P. Haffter, M. Hammerschmidt, D. A. Kane, R. N.
973 Kelsh, M. C. Mullins, J. Odenthal, R. M. Warga and C. Nusslein-Volhard (1996). "Jaw and
974 branchial arch mutants in zebrafish II: anterior arches and cartilage differentiation."
975 Development **123**: 345-356.

976 Rabadan, M. A., A. Herrera, L. Fanlo, S. Usieto, C. Carmona-Fontaine, E. H. Barriga, R. Mayor, S.
977 Pons and E. Marti (2016). "Delamination of neural crest cells requires transient and reversible
978 Wnt inhibition mediated by Dact1/2." Development **143**(12): 2194-2205.

979 Ran, F. A., P. D. Hsu, J. Wright, V. Agarwala, D. A. Scott and F. Zhang (2013). "Genome
980 engineering using the CRISPR-Cas9 system." Nat Protoc **8**(11): 2281-2308.

981 Reynolds, K., P. Kumari, L. Sepulveda Rincon, R. Gu, Y. Ji, S. Kumar and C. J. Zhou (2019). "Wnt
982 signaling in orofacial clefts: crosstalk, pathogenesis and models." Dis Model Mech **12**(2).

983 Ribes, V., N. Balaskas, N. Sasai, C. Cruz, E. Dessaud, J. Cayuso, S. Tozer, L. L. Yang, B. Novitch, E.
984 Marti and J. Briscoe (2010). "Distinct Sonic Hedgehog signaling dynamics specify floor plate and
985 ventral neuronal progenitors in the vertebrate neural tube." Genes Dev **24**(11): 1186-1200.

986 Rochard, L., S. D. Monica, I. T. Ling, Y. Kong, S. Roberson, R. Harland, M. Halpern and E. C. Liao
987 (2016). "Roles of Wnt pathway genes wls, wnt9a, wnt5b, frzb and gpc4 in regulating
988 convergent-extension during zebrafish palate morphogenesis." Development **143**(14): 2541-
989 2547.

990 Rossi, A., Z. Kontarakis, C. Gerri, H. Nolte, S. Holper, M. Kruger and D. Y. Stainier (2015).
991 "Genetic compensation induced by deleterious mutations but not gene knockdowns." Nature
992 **524**(7564): 230-233.

993 Sander, J. D., P. Zaback, J. K. Joung, D. F. Voytas and D. Dobbs (2007). "Zinc Finger Targeter
994 (ZiFiT): an engineered zinc finger/target site design tool." Nucleic Acids Res **35**(Web Server
995 issue): W599-605.

996 Schilling, T. F. and P. Le Pabic (2009). "Fishing for the signals that pattern the face." J Biol **8**(11):
997 101.

998 Schubert, F. R., D. R. Sobreira, R. G. Janousek, L. E. Alvares and S. Dietrich (2014). "Dact genes
999 are chordate specific regulators at the intersection of Wnt and Tgf-beta signaling pathways."
1000 BMC Evol Biol **14**: 157.

1001 Shi, D. L. (2022). "Wnt/planar cell polarity signaling controls morphogenetic movements of
1002 gastrulation and neural tube closure." Cell Mol Life Sci **79**(12): 586.

1003 Sisson, B. E., R. M. Dale, S. R. Mui, J. M. Topczewska and J. Topczewski (2015). "A role of
1004 glypican4 and wnt5b in chondrocyte stacking underlying craniofacial cartilage morphogenesis."
1005 Mech Dev **138 Pt 3**: 279-290.

1006 Solnica-Krezel, L., D. L. Stemple, E. Mountcastle-Shah, Z. Rangini, S. C. Neuhauss, J. Malicki, A. F.
1007 Schier, D. Y. Stainier, F. Zwartkruis, S. Abdelilah and W. Driever (1996). "Mutations affecting cell
1008 fates and cellular rearrangements during gastrulation in zebrafish." Development **123**: 67-80.

1009 Song, N., K. Cui, L. Zeng, Y. Fan, Z. Wang, P. Shi, W. Su and H. Wang (2024). "Calpain 8 as a
1010 potential biomarker regulates the progression of pancreatic cancer via EMT and AKT/ERK
1011 pathway." J Proteomics **301**: 105182.

1012 Sorimachi, H., S. Ishiura and K. Suzuki (1993). "A novel tissue-specific calpain species expressed
1013 predominantly in the stomach comprises two alternative splicing products with and without
1014 Ca(2+)-binding domain." J Biol Chem **268**(26): 19476-19482.

1015 Steinhart, Z. and S. Angers (2018). "Wnt signaling in development and tissue homeostasis."
1016 Development **145**(11).

1017 Su, Y., L. Zhang, X. Gao, F. Meng, J. Wen, H. Zhou, A. Meng and Y. G. Chen (2007). "The
1018 evolutionally conserved activity of Dapper2 in antagonizing TGF-beta signaling." FASEB J **21**(3):
1019 682-690.

1020 Swartz, M. E., K. Sheehan-Rooney, M. J. Dixon and J. K. Eberhart (2011). "Examination of a
1021 palatogenic gene program in zebrafish." Dev Dyn **240**(9): 2204-2220.

1022 Tada, M. and C. P. Heisenberg (2012). "Convergent extension: using collective cell migration
1023 and cell intercalation to shape embryos." Development **139**(21): 3897-3904.

1024 Thisse, B., Pflumio, S., Furthauer, M., Loppin, B., Heyer, V., Degrave, A., Woehl, R., Lux, A.,
1025 Steffan, T., Charbonnier, X.Q., Thisse, C. (2001). "Expression of the zebrafish genome during
1026 embryogenesis." from http://zfin.org.

1027 Topczewski, J., D. S. Sepich, D. C. Myers, C. Walker, A. Amores, Z. Lele, M. Hammerschmidt, J.
1028 Postlethwait and L. Solnica-Krezel (2001). "The zebrafish glypican knypek controls cell polarity
1029 during gastrulation movements of convergent extension." Dev Cell **1**(2): 251-264.

1030 Wada, N., Y. Javidan, S. Nelson, T. J. Carney, R. N. Kelsh and T. F. Schilling (2005). "Hedgehog
1031 signaling is required for cranial neural crest morphogenesis and chondrogenesis at the midline
1032 in the zebrafish skull." Development **132**(17): 3977-3988.

1033 Walker, M. B. and C. B. Kimmel (2007). "A two-color acid-free cartilage and bone stain for
1034 zebrafish larvae." Biotech Histochem **82**(1): 23-28.

1035 Waxman, J. S., A. M. Hocking, C. L. Stoick and R. T. Moon (2004). "Zebrafish Dapper1 and
1036 Dapper2 play distinct roles in Wnt-mediated developmental processes." Development **131**(23):
1037 5909-5921.

1038 Wen, J., Y. J. Chiang, C. Gao, H. Xue, J. Xu, Y. Ning, R. J. Hodes, X. Gao and Y. G. Chen (2010).
1039 "Loss of Dact1 disrupts planar cell polarity signaling by altering dishevelled activity and leads to
1040 posterior malformation in mice." J Biol Chem **285**(14): 11023-11030.

1041 Westerfield, M. (1993). The zebrafish book : a guide for the laboratory use of zebrafish
1042 (Brachydanio rerio). Eugene, OR, M. Westerfield.

1043 Wiese, K. E., R. Nusse and R. van Amerongen (2018). "Wnt signalling: conquering complexity."
1044 Development **145**(12).

1045 Wong, H. C., A. Bourdelas, A. Krauss, H. J. Lee, Y. Shao, D. Wu, M. Mlodzik, D. L. Shi and J. Zheng
1046 (2003). "Direct binding of the PDZ domain of Dishevelled to a conserved internal sequence in
1047 the C-terminal region of Frizzled." Mol Cell **12**(5): 1251-1260.

1048 Wu, T., E. Hu, S. Xu, M. Chen, P. Guo, Z. Dai, T. Feng, L. Zhou, W. Tang, L. Zhan, X. Fu, S. Liu, X.
1049 Bo and G. Yu (2021). "clusterProfiler 4.0: A universal enrichment tool for interpreting omics
1050 data." Innovation (Camb) **2**(3): 100141.

1051 Zanardelli, S., N. Christodoulou and P. A. Skourides (2013). "Calpain2 protease: A new member
1052 of the Wnt/Ca(2+) pathway modulating convergent extension movements in Xenopus." Dev Biol
1053 **384**(1): 83-100.

1054 Zhang, J., W. S. Talbot and A. F. Schier (1998). "Positional cloning identifies zebrafish one-eyed
1055 pinhead as a permissive EGF-related ligand required during gastrulation." Cell **92**(2): 241-251.

1056 Zhang, L., X. Gao, J. Wen, Y. Ning and Y. G. Chen (2006). "Dapper 1 antagonizes Wnt signaling by
1057 promoting dishevelled degradation." J Biol Chem **281**(13): 8607-8612.

1058 Zhang, L., H. Zhou, Y. Su, Z. Sun, H. Zhang, L. Zhang, Y. Zhang, Y. Ning, Y. G. Chen and A. Meng
1059 (2004). "Zebrafish Dpr2 inhibits mesoderm induction by promoting degradation of nodal
1060 receptors." Science **306**(5693): 114-117.

1061 Zheng, G. X., J. M. Terry, P. Belgrader, P. Ryvkin, Z. W. Bent, R. Wilson, S. B. Ziraldo, T. D.
1062 Wheeler, G. P. McDermott, J. Zhu, M. T. Gregory, J. Shuga, L. Montesclaros, J. G. Underwood, D.
1063 A. Masquelier, S. Y. Nishimura, M. Schnall-Levin, P. W. Wyatt, C. M. Hindson, R. Bharadwaj, A.

1064 Wong, K. D. Ness, L. W. Beppu, H. J. Deeg, C. McFarland, K. R. Loeb, W. J. Valente, N. G. Ericson,
1065 E. A. Stevens, J. P. Radich, T. S. Mikkelsen, B. J. Hindson and J. H. Bielas (2017). "Massively
1066 parallel digital transcriptional profiling of single cells." Nat Commun **8**: 14049.

1067 Zhong, X., S. Xu, Q. Wang, L. Peng, F. Wang, T. He, C. Liu, S. Ni and Z. He (2022). "CAPN8 involves
1068 with exhausted, inflamed, and desert immune microenvironment to influence the metastasis of
1069 thyroid cancer." Front Immunol **13**: 1013049.

1070 Zhu, A., J. G. Ibrahim and M. I. Love (2019). "Heavy-tailed prior distributions for sequence count
1071 data: removing the noise and preserving large differences." Bioinformatics **35**(12): 2084-2092.
1072

1073

1074

1075

1076

1077

1078

1079

1080

1081

1082

1083

1084

1085

1086

1087

1088

1089

Figure Legends

Figure 1. Unique and shared *dact1* and *dact2* gene expression domains during zebrafish development. **(A-C)** Representative images of wholemount *in situ* hybridization showing *dact1*, *dact2,* and *wnt11f2* gene expression patterns. **A)** At 8 hpf, *dact2* and *wnt11f2* are highly expressed in the dorsal margin and presumptive Nieuwkoop center of the gastrulating embryo, with *dact1* being weakly detected (arrowhead). In contrast to *wnt11f2*, *dact1* and *dact2* are expressed in the presumptive dorsal mesoderm (asterisk). **B)** Lateral (anterior to the left of page) and anterior (dorsal side toward top of page) views of bud-stage embryos. *dact2* and *wnt11f2* transcripts are detected in the anterior neural plate (arrowhead) and tailbud (asterisk) while *dact2* is additionally expressed in the axial mesoderm (arrow). *dact1* gene expression is concentrated to the paraxial mesoderm (open arrowhead). **C)** Lateral and flat-mount views of 4 ss embryos. *dact2* is expressed in the anterior neural plate and polster (P), notochord (N), paraxial and presomitic mesoderm (PM) and tailbud (TB). *wnt11f2* is also expressed in these cells (Thisse, Pflumio et al. 2001). In contrast, *dact1* is expressed in the midbrain (MP) and the paraxial and presomitic mesoderm. (**D-E)** Representative lateral (anterior to left of page) images of wholemount *in situ* hybridization showing *dact1* and *dact2* expression patterns. **D)** At 24 hpf expression is detected in the developing head. **E)** At 48 hpf expression is detected in the developing craniofacial structures (arrow). **F)** Representative images of RNAscope *in situ* hybridization analysis of *dact1* (white) and *dact2* (yellow) and *irf6* (green) expression in transverse section of 72 hpf embryos. *dact1* is expressed in the ethmoid plate (ep) and palatoquadrate (pq)

orofacial cartilage, while *dact2* is expressed in the oral epithelium (oe). The epithelial marker *irf6* is expressed in the oe and surface epithelium (se). Dapi (blue). Scale bar: 100 μm.

Figure 2. Impaired convergent extension in *dact1* and *dact2* compound mutants. **A)** Inter-cross of compound heterozygotes yield embryos with different degrees of axis extension that correspond to the *dact1* and *dact2* genotypes. Representative lateral images of embryos at 12 hpf. The yellow line indicates body axis angle measured from the anterior point of the head, the center of the yolk, to the end of the tail. **B)** Quantification of body axis angle. Numbers represent the difference in angle relative to the average wildtype embryo. Asterisk indicates genotypes with angles significantly different from wildtype. ANOVA $p<0.5$ n= 3-21 embryos. **C)** Representative bud stage wildtype and *dact1-/-,dact2-/-* mutant embryos stained for *gsc* (prechordal plate), *pax2a* (midbrain/hindbrain boundary) and *krox20* (rhombomere 3). Asterisk indicates lack of *krox20* expression in *dact1-/-,dact2-/-* mutant. Scale bar = 200 μm **D)** Representative flat mounts of 1-2 ss wildtype and *dact1/2* mutant embryos stained for *zic1* (telencephalon), *pax2a* and *tbx6* (ventrolateral mesoderm). **E)** Representative flat mounts of 10 ss wildtype and *dact1/2-/-* mutant embryos stained for *ctsl1b* (hatching gland), *zic1*, *pax2a*, *krox20*, and *myo1d* (somites).

Figure 3. Midface development requires *dact1* and *dact2*. **A)** Representative brightfield images of wildtype and *dact1/2-/-* compound mutants at 4 dpf. 100 individuals were analyzed from a *dact1*+/-,*dact2*+/- double het cross. Lateral and ventral views show

d*act1/2-/-* compound mutants have a hypoplastic midface, medially displaced eyes, and a displaced lower jaw. **B)** Representative flat-mount images of Alcian blue stained ethmoid plate (EP) and visceral cartilage (VC) elements from 4 dpf wildtype and d*act1/2-/-* compound mutants. d*act1/2-/-* mutants have a rod-shaped EP with no distinct lateral and medial elements. No obvious differences were found in *dact1/2* mutant VC. **C)** Representative brightfield image of 4 dpf wildtype and *dact1/2-/-* mutant. Bar indicates vertebral spine length. Scale bar: 100 μm. **D)** Representative images of wildtype and dact1/2-/- mu Alcian blue stained *dact1/2-/-*, *wnt11f2-/-,* and *wnt11f2-/-* ,*dact1*/*2*-/- compound mutants. Embryos resulted from a *dact1*+/-,*dact2*+/-,*wnt11f2*+/- in-cross. Lateral and ventral views show similar craniofacial phenotypes in each mutant. **E)** Representative flat-mount images of Alcian blue stained EP show a similar phenotype between *dact1/2-/-*, *wntllf2-/-,* and *wnt11f2-/-,dact1/2-*/- compound mutants. Scale bar: 200 μm.

Figure 4. Anterior neural crest cells of the *dact1/2-/-* mutant migrate to the midline and populate the dysmorphic ethmoid plate. Lineage tracing of wildtype and *dact1/2-/-* double mutant zebrafish embryos using Tg(*sox10*:kaede) line. *sox10*:kaede fluorescence is shown in green and photo-converted kaede is shown in magenta and highlighted with an arrow. Asterisks indicate that the cell population is absent. **A,B)**19 hpf embryo sagittal views showing photoconversion of anterior-most neural crest population. At 36 hpf frontal images show the migration of photoconverted neural crest cells to the frontal prominence in wildtype and *dact1/2-/-* double mutants. At 55 hpf, frontal images show photoconverted neural crest cells populating the region of the

developing ANC in wildtype and *dact1/2-/-* mutants. At 4.5 dpf ventral images show photoconverted neural crest cells populating the medial ethmoid plate in wildtype. Similarly, neural crest cells in *dact1/dact2-/-* mutants populate the rod-shaped ethmoid plate. Scale bar:100 μm. Representative images of 3 individual experiments.

Figure 5. A nonoverlapping functional role for *dact1*, *dact2,* and *gpc4* and *wls*. **A)** Representative Alcian blue stained wholemount images of wildtype, *dact1/2-/-* double mutant, *gpc4-/-* mutant, and *gpc4-/-,dact1/2-/-* triple mutants at 4 dpf. Low magnification lateral images of embryos showing tail truncation in *dact1/2-/-* mutants, shortened and kinked tail in *gpc4-/-* mutants, and a combinatorial effect in *gpc4-/-,dact1/2-/-* triple mutants. Higher magnification lateral images show a shortened midface and displaced lower jaw in *dact1/2-/-* mutants, a shortened midface in *gpc4-/-* mutant, and a combinatorial effect in *gpc4-/-,dact1/2-/-* triple mutants. **B)** Representative flat-mount images of dissected Alcian blue-stained cartilage elements. *dact1/2-/-* mutants have a narrow rod-shaped ethmoid plate (EP) while *gpc4-/-* mutants have a broad and shortened EP. *dact1/2/gpc4* triple mutants have a combinatorial effect with a short, broad rod-shaped EP. In ventral cartilages (VC), *dact1/2-/-* mutants have a relatively normal morphology while Meckel's cartilage in *gpc4-/-* mutants and *gpc4-/-,dact1/2-/-* triple mutants is truncated. **C,D)** Same as above except *wls-/-* mutant and *wls-/-,dact1/2-/-* triple mutant, with similar findings. **E)** Combinatorial genotypes of *dact1*, *dact2,* and *gpc4*. *dact2*-/- contributed the *dact/gpc4* compound phenotype while *dact1-/-* did not. Scale bar: 200 μm.

Figure 6. Single-cell RNAseq of 4 ss wildtype, *dact1/2-/-* mutant and *gpc4-/-* mutants. **A)** Summary schematic showing similar phenotypes in *dact1/2-/-* and *gpc4-/-* mutants at 12 hpf and divergent phenotypes at 4 dpf. Single-cell RNAseq was performed during axis extension to compare and contrast *dact1/2-/-* and *gpc4-/-* transcriptional programs. UMAP showing cluster identification. **B)** UMAP of cell clusters identified by Single-cell RNAseq. **C)** Dot plot showing the most differentially expressed genes between clusters. **D)** UMAP showing *dact1*, *dact2,* and *gpc4* expression in wildtype embryos.

Figure 7. Pseudobulk differential expression analysis of single-cell RNAseq data. **A)** Heatmaps showing the 50 most differentially expressed genes in 3 major cell types; ectoderm (clusters 4,5,6,7), paraxial mesoderm (clusters 10,11,12), and lateral plate mesoderm (clusters 15, 16, 17,18) between *dact1/2-/-* mutants and wildtype and *gpc4-/-* mutants and wildtype. **B)** Venn diagrams showing unique and overlapping DEGs in *dact1/2-/-* and *gpc4-/-* mutants. **C)** GO analysis of *dact1/2-/-* mutant-specific DEGs in lateral plate mesoderm showing enrichment for proteolytic processes.

Figure 8. Expression of *capn8* is significantly dysregulated in *dact1/2-/-* mutants. **A)** Single-cell RNAseq gene expression analysis of *capn8* in wildtype and *dact1/2-/-* mutants. In wildtype embryos, *capn8* expression is restricted predominantly to the epidermis whereas *capn8* is widely expressed throughout the embryo in *dact1/2-/-* mutants, especially in the mesoderm. **B)** Wholemount *in situ* hybridization of *capn8* expression in wildtype and *dact1/2-/-* mutant embryos at 2 ss. Staining corroborates the single-cell RNAseq data, with expanded ectopic expression of *capn8* throughout the

embryo**.** Flat mounts are oriented anterior to the left. Scale bar: 100 μm. **C)** Brightfield images and alcian blue staining of the ethmoid plate show ectopic expression of *capn8* mRNA (200 pg) at the 1-cell stage in *dact1+/-*,*dact2+/-* embryos recapitulates the *dact1/2-/-* compound mutant craniofacial phenotype. The mutant craniofacial phenotype did not manifest in gfp mRNA (200 pg) injected 1-cell stage *dact1+/-*,*dact2+/-* embryos. Scale bar: 100 μm **D)** Quantification of mutant and normal craniofacial phenotype in 4 dpf larvae after mRNA injection at the 1-cell stage. Larvae were derived from *dact1+/-*,*dact2+/-* interbreeding. Larvae were uninjected or injected with 200 pg *gfp* control or *capn8* mRNA. A Fisher exact test showed a significant effect of *capn8* mRNA injecting in the *dact1/2* double heterozygotes. p= 0.013.

Supplemental Figures

Figure S1. Daniocell single-cell RNAseq analysis with a display of *dact1*, *dact2*, *gpc4,* and *wnt11f2* in all cell clusters from 3-120 hpf of development (Farrell, Wang et al. 2018). Cephalic mesoderm (ceph mes), mesenchyme, neural ectoderm, and muscle clusters are noted.

Figure S2. Characterization of CRISPR/Cas9 generated *dact1-/-* and *dact2-/-* mutants. **A)** Schematic representations of *dact1* and *dact2* exons, positions of guide RNA target site, introduced premature stop codon (arrow), and sequences of mutations. **B)** DNA fragment analysis of *dact1+/-* and *dact2+/-* animals showing wildtype (250 and 387 bp respectively and mutant (228 and 380 bp respectively) **C)** Expression levels of *dact1*

and *dact2* mRNA by RT-qPCR in 12 hpf *dact1-/-* mutants, *dact2-/-* mutants, and *dact1/2-/-* compound mutants. 8 embryos were pooled for mRNA isolation per sample. **D)** Injection of *dact1* mRNA, *dact2* mRNA, or a combination of *dact1* and *dact2* mRNA rescues the rod-shaped ethmoid plate phenotype in *dact1/2-/-* compound mutants. Representative images of Alcian blue stained *dact1/2-/-* double mutant treated with 300 pg *dact1* mRNA and 300 pg *dact2* mRNA. Arrow highlights normal ethmoid plate (EP). Visceral cartilage (VC) also appeared normal. **E)** Quantification of the mutant craniofacial phenotype observed in a *dact1-/-,dact2+/-* breeding in-cross. Without mRNA injection, the mutant phenotype was observed at approximately (35%) the expected Mendelian ratio of 25%. Injection with *dact1* mRNA, *dact2* mRNA, or a combination of *dact1* and *dact2* mRNA decreased the frequency that the mutant craniofacial phenotype was observed.

Figure S3. Loss of *dact1* and *dact2* tends to decrease total body length. **A)** Representative brightfield images of 4 dpf larvae of compound *dact1* and *dact2* mutant genotypes. Bar represents *dact1+/+,dact2+/+* body length measurement. Scale bar: 100 μm. **B)** Scatter plot of body length measurement of compound *dact1* and *dact2* mutant genotypes at 4 dpf. ANOVA p=0.06. n=3-4.

Figure S4. Cluster abundance across genotype groups. Scatter box plots showing the frequency of each identified cell cluster between *dact1/2-/-*, *gpc4-/-*, and wildtype samples.

Figure S5. Loss of *gpc4* and loss of *dact1/2* leads to distinct changes in gene expression profiles but with some overlapping functions. GO analysis of DEGs identified between *gpc4*-/- and wildtype embryos and *dact1/2*-/- and wildtype embryos found changes in calcium ion binding and actin interaction in both mutants.

Figure 1

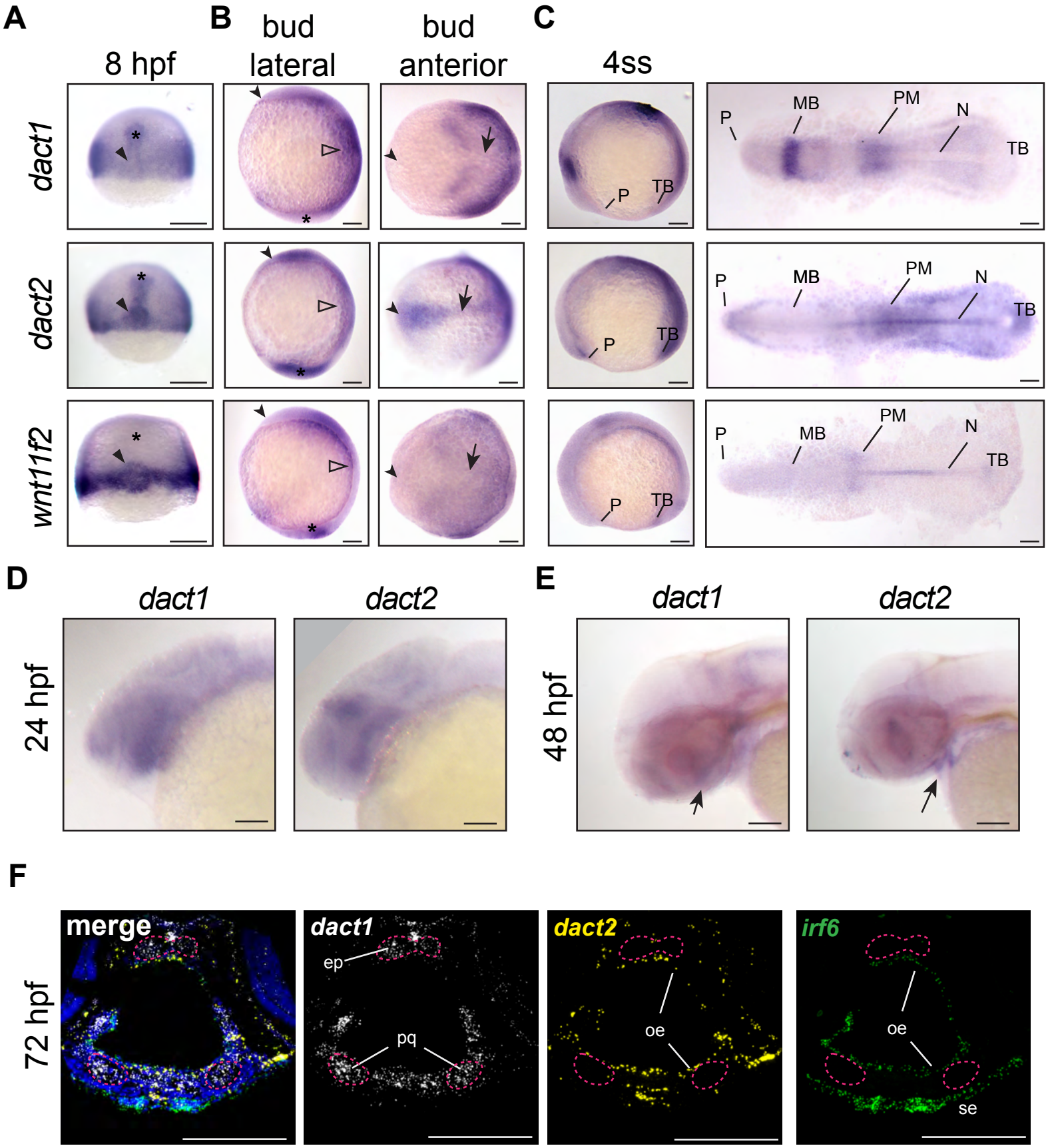
A
B
C
8 hpf
bud lateral
bud anterior
4ss
dact1
dact2
wnt11f2
P
MB
PM
N
TB
D
E
dact1
dact2
24 hpf
48 hpf
F
72 hpf
merge
dact1
dact2
irf6
ep
pq
oe
se

Figure 2

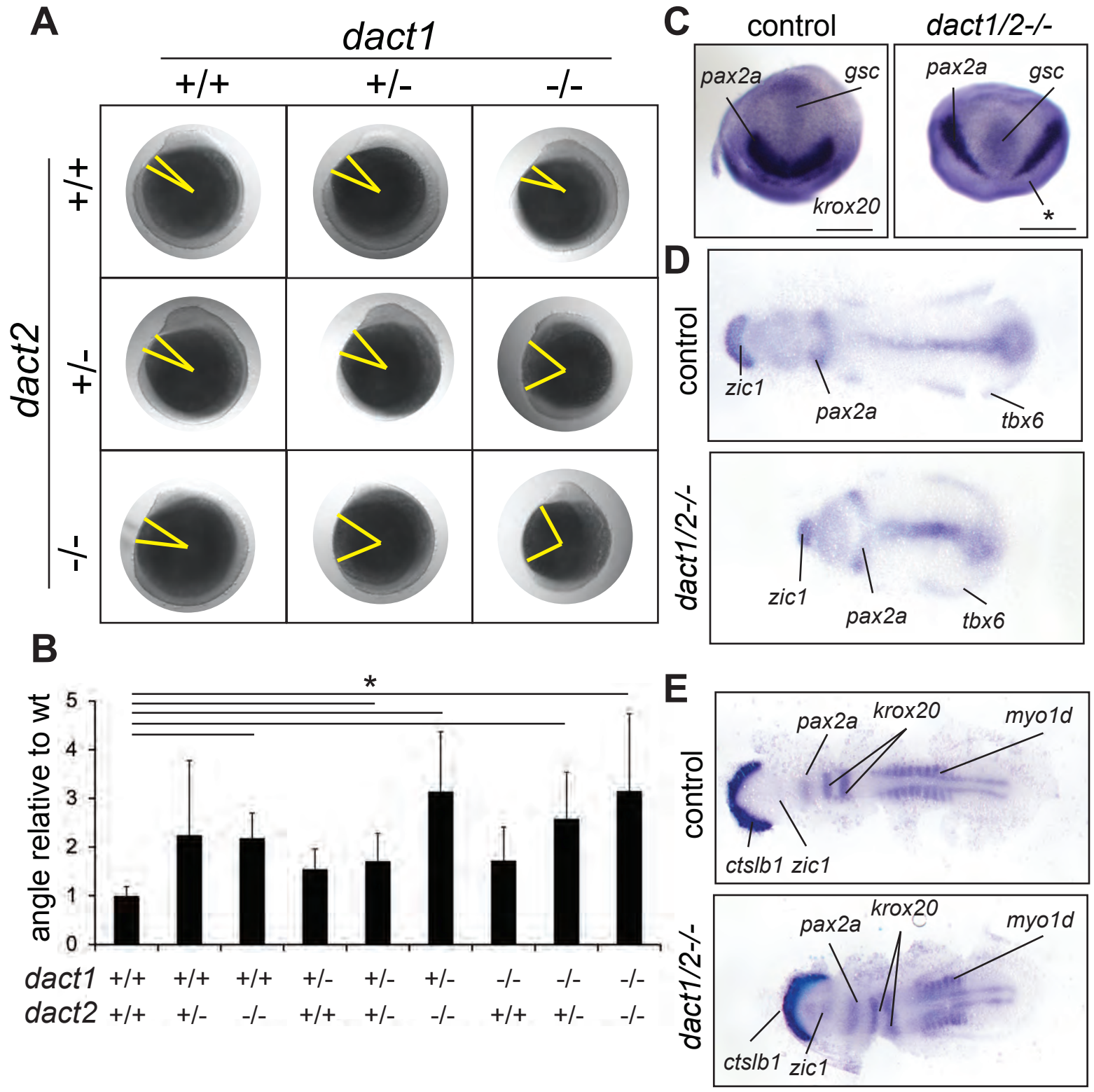
A
dact1
+/+
+/-
-/-
dact2
+/+
+/-
-/-
B
angle relative to wt
0
1
2
3
4
5
*
dact1 +/+ +/+ +/+ +/- +/- +/- -/- -/- -/-
dact2 +/+ +/- -/- +/+ +/- -/- +/+ +/- -/-
C
control
dact1/2-/-
pax2a
gsc
krox20
pax2a
gsc
*
D
control
zic1
pax2a
tbx6
dact1/2-/-
zic1
pax2a
tbx6
E
control
pax2a
krox20
myo1d
ctslb1
zic1
dact1/2-/-
pax2a
krox20
myo1d
ctslb1
zic1

Figure 3

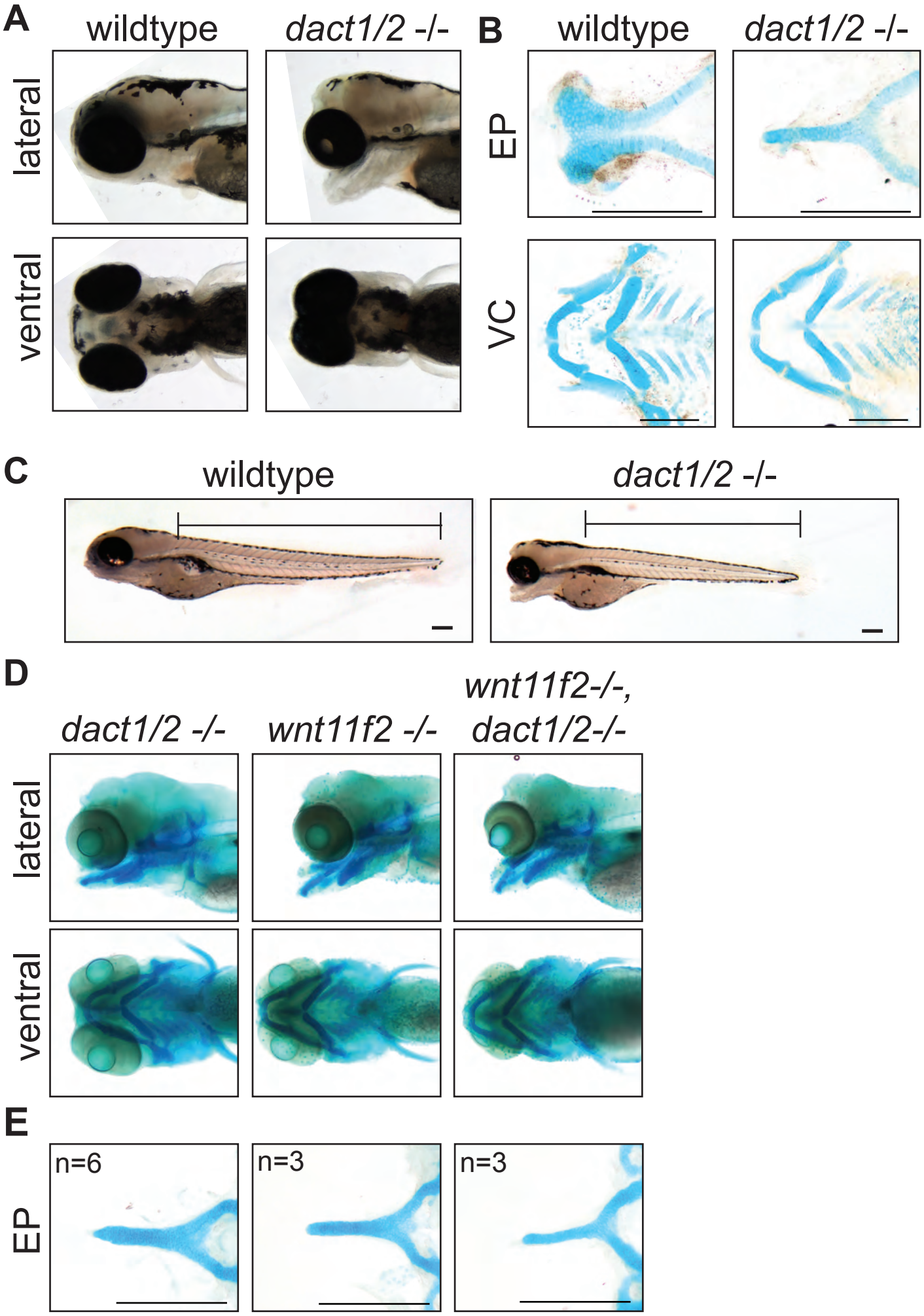
A
wildtype
dact1/2 -/-
lateral
ventral
B
wildtype
dact1/2 -/-
EP
VC
C
wildtype
dact1/2 -/-
D
dact1/2 -/-
wnt11f2 -/-
wnt11f2-/-,
dact1/2-/-
lateral
ventral
E
EP
n=6
n=3
n=3

Figure 4

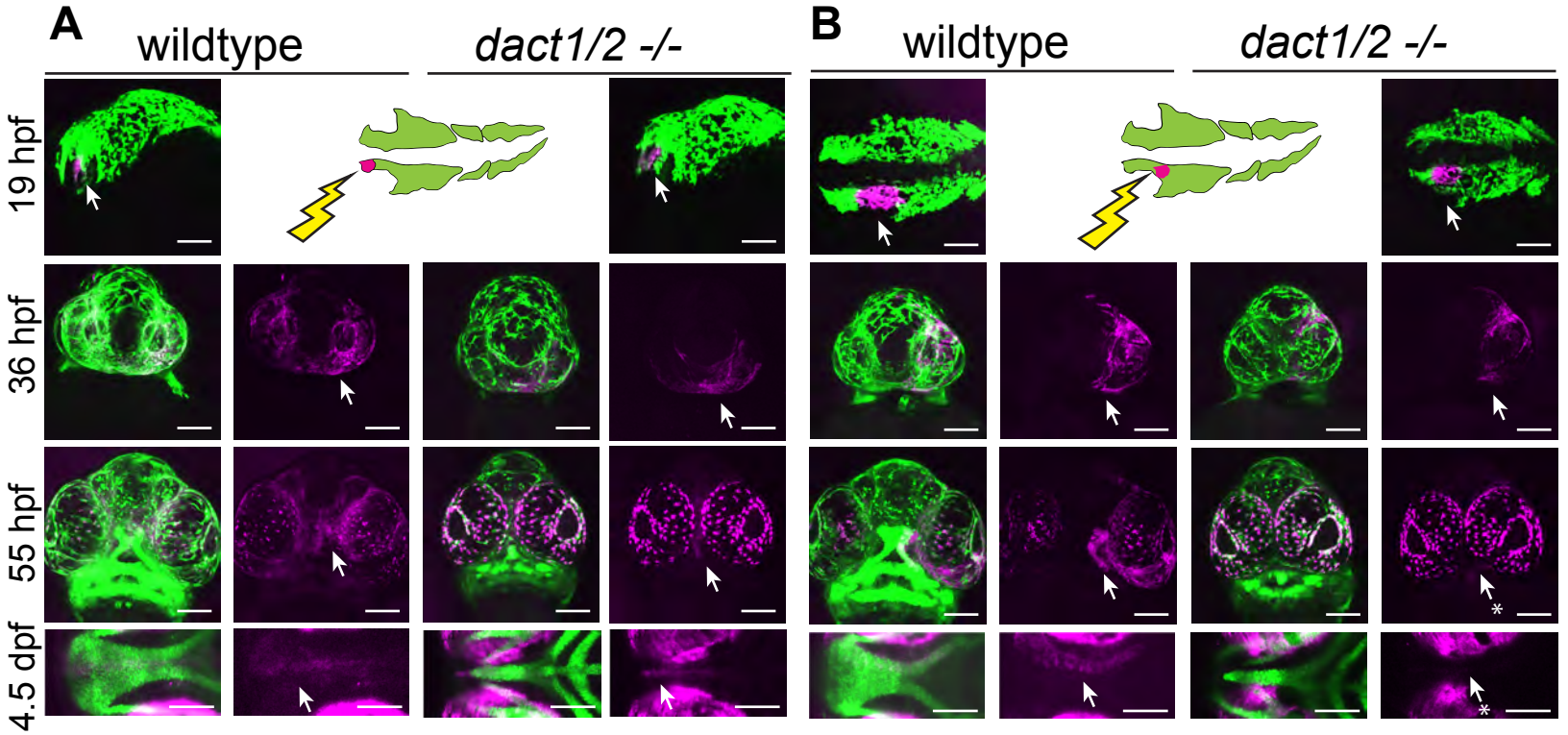
A
wildtype
dact1/2 -/-
B
wildtype
dact1/2 -/-
19 hpf
36 hpf
55 hpf
4.5 dpf

Figure 5

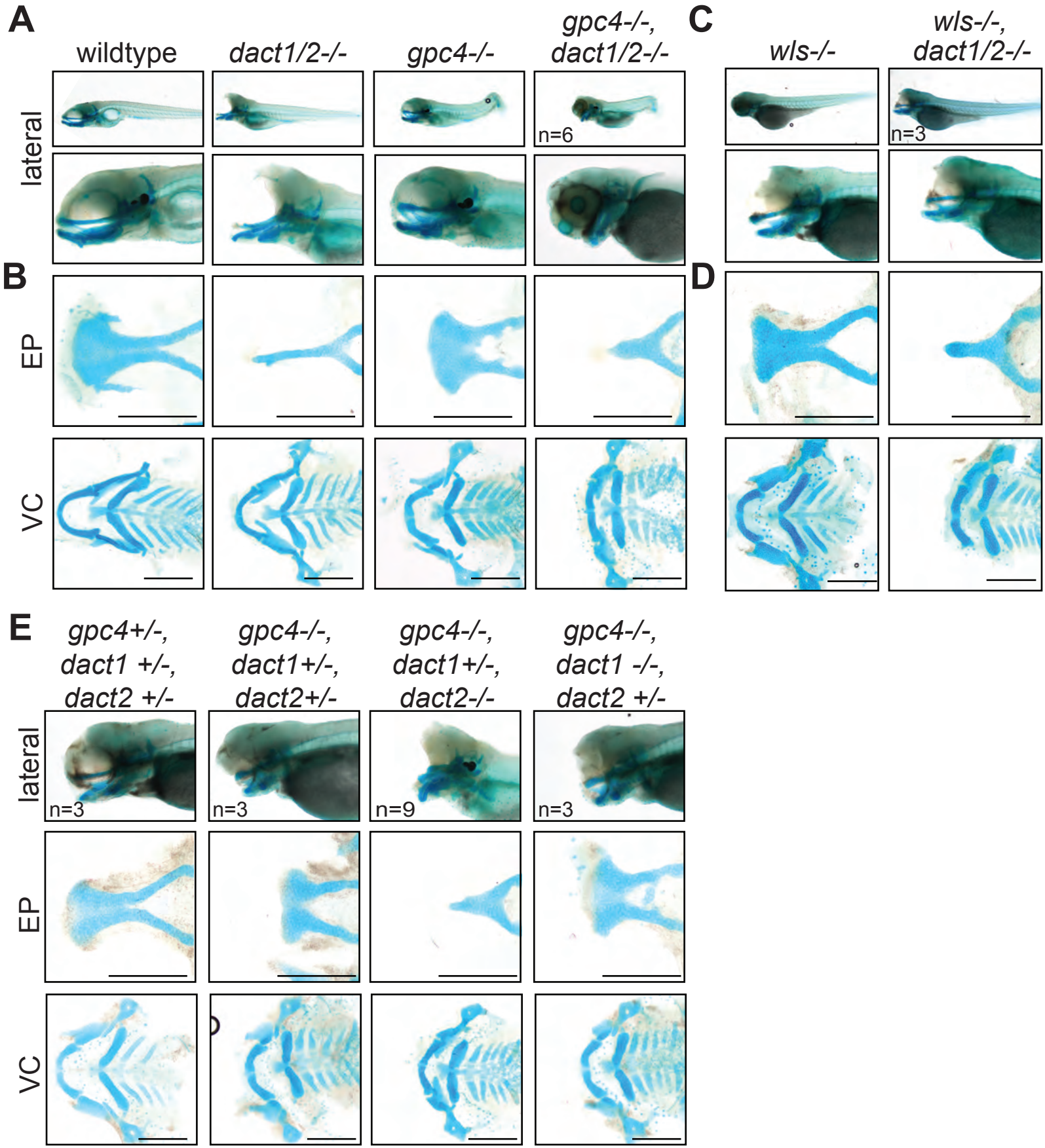
A
wildtype
dact1/2-/-
gpc4-/-
gpc4-/-, dact1/2-/-
lateral
n=6
B
EP
VC
C
wls-/-
wls-/-, dact1/2-/-
n=3
D
E
gpc4+/-, dact1 +/-, dact2 +/-
gpc4-/-, dact1+/-, dact2+/-
gpc4-/-, dact1+/-, dact2-/-
gpc4-/-, dact1 -/-, dact2 +/-
lateral
n=3
n=3
n=9
n=3
EP
VC

Figure 6

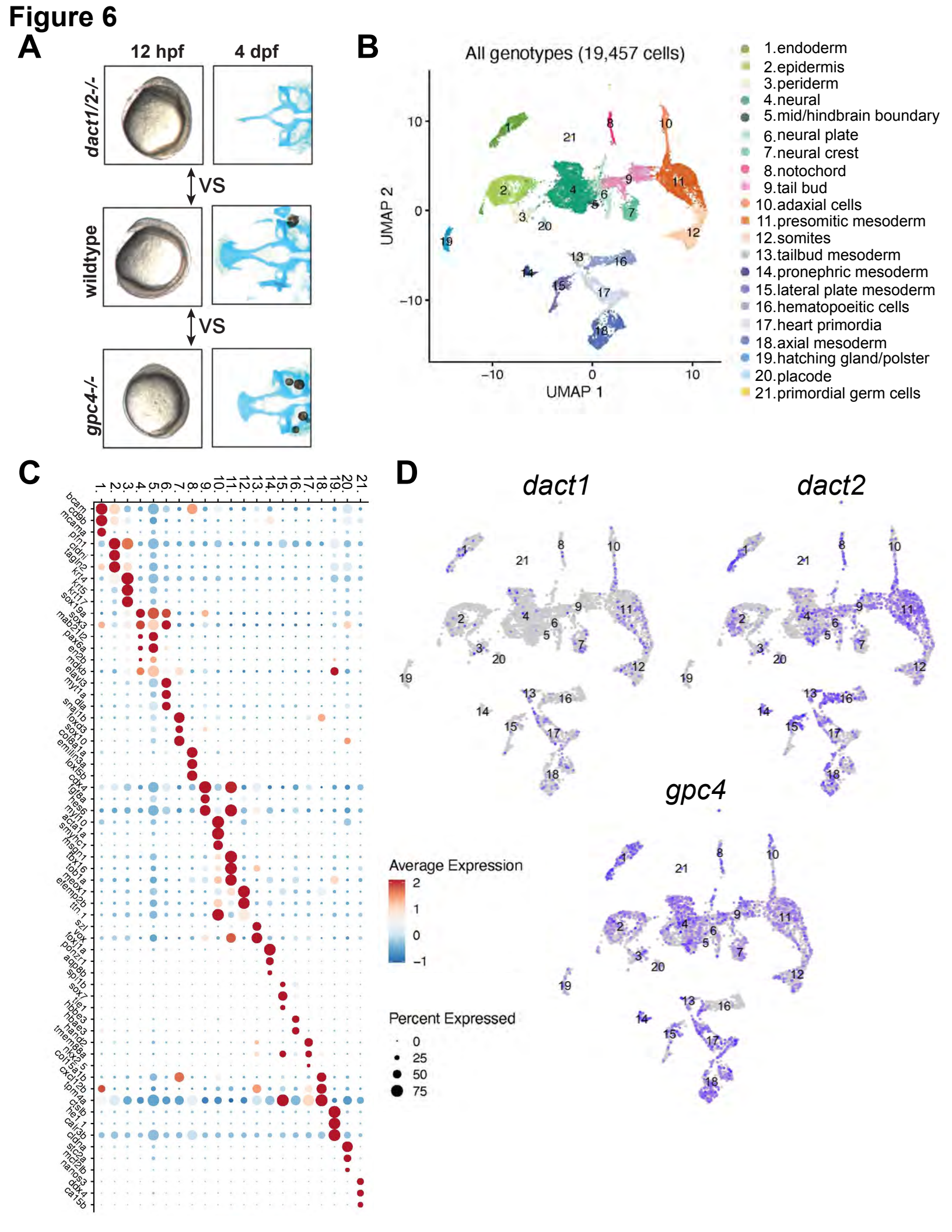
A
12 hpf
4 dpf
dact1/2-/-
VS
wildtype
VS
gpc4-/-
B
All genotypes (19,457 cells)
UMAP 2
UMAP 1
1.endoderm
2.epidermis
3.periderm
4.neural
5.mid/hindbrain boundary
6.neural plate
7.neural crest
8.notochord
9.tail bud
10.adaxial cells
11.presomitic mesoderm
12.somites
13.tailbud mesoderm
14.pronephric mesoderm
15.lateral plate mesoderm
16.hematopoeitic cells
17.heart primordia
18.axial mesoderm
19.hatching gland/polster
20.placode
21.primordial germ cells
C
D
dact1
dact2
gpc4
Average Expression
Percent Expressed

Figure 7

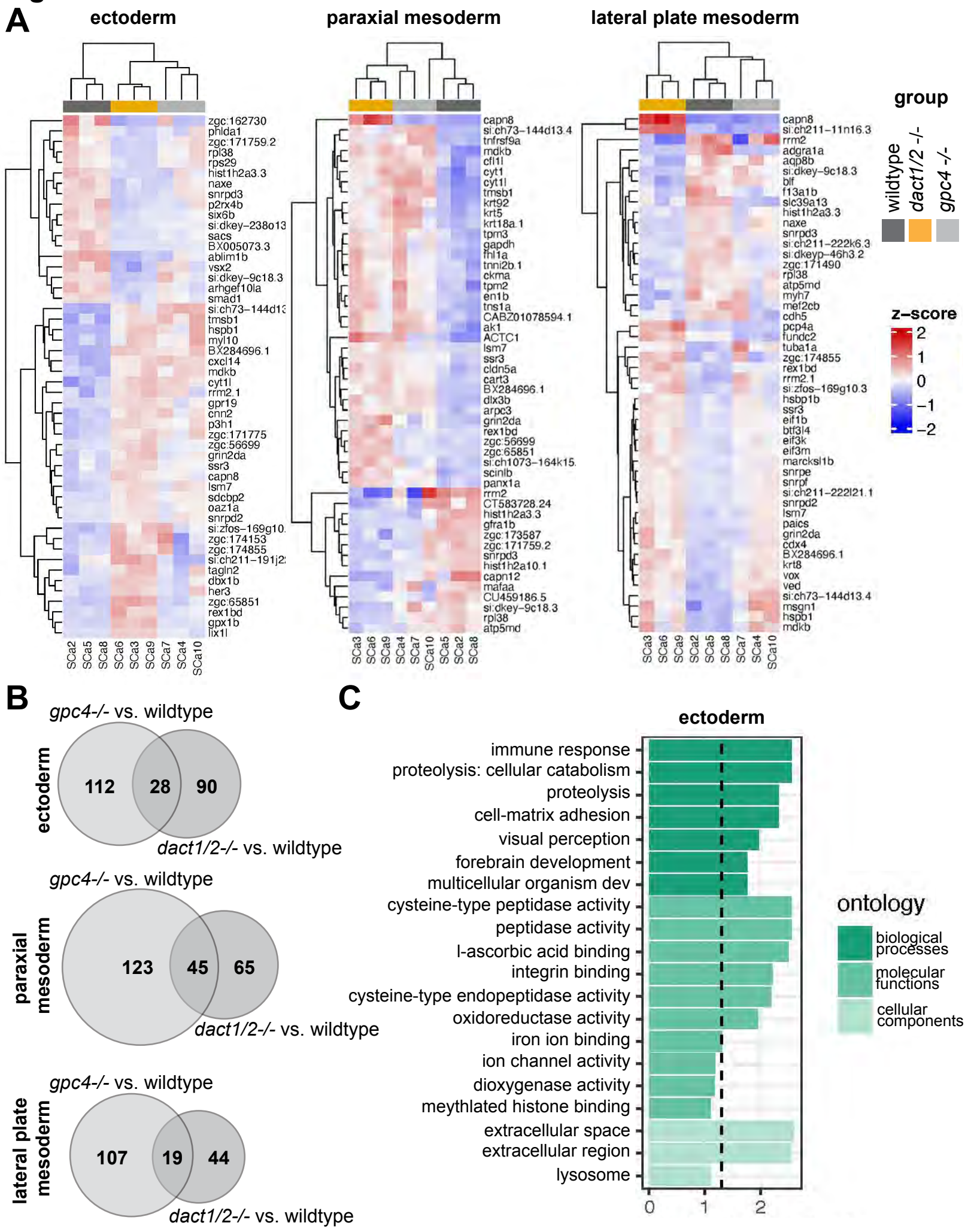
A
ectoderm
paraxial mesoderm
lateral plate mesoderm
group
wildtype
dact1/2 -/-
gpc4 -/-
z-score
2
1
0
−1
−2
B
gpc4-/- vs. wildtype
ectoderm
112
28
90
dact1/2-/- vs. wildtype
gpc4-/- vs. wildtype
paraxial mesoderm
123
45
65
dact1/2-/- vs. wildtype
gpc4-/- vs. wildtype
lateral plate mesoderm
107
19
44
dact1/2-/- vs. wildtype
C
ectoderm
immune response
proteolysis: cellular catabolism
proteolysis
cell-matrix adhesion
visual perception
forebrain development
multicellular organism dev
cysteine-type peptidase activity
peptidase activity
l-ascorbic acid binding
integrin binding
cysteine-type endopeptidase activity
oxidoreductase activity
iron ion binding
ion channel activity
dioxygenase activity
meythlated histone binding
extracellular space
extracellular region
lysosome
0
1
2
ontology
biological processes
molecular functions
cellular components

Figure 8

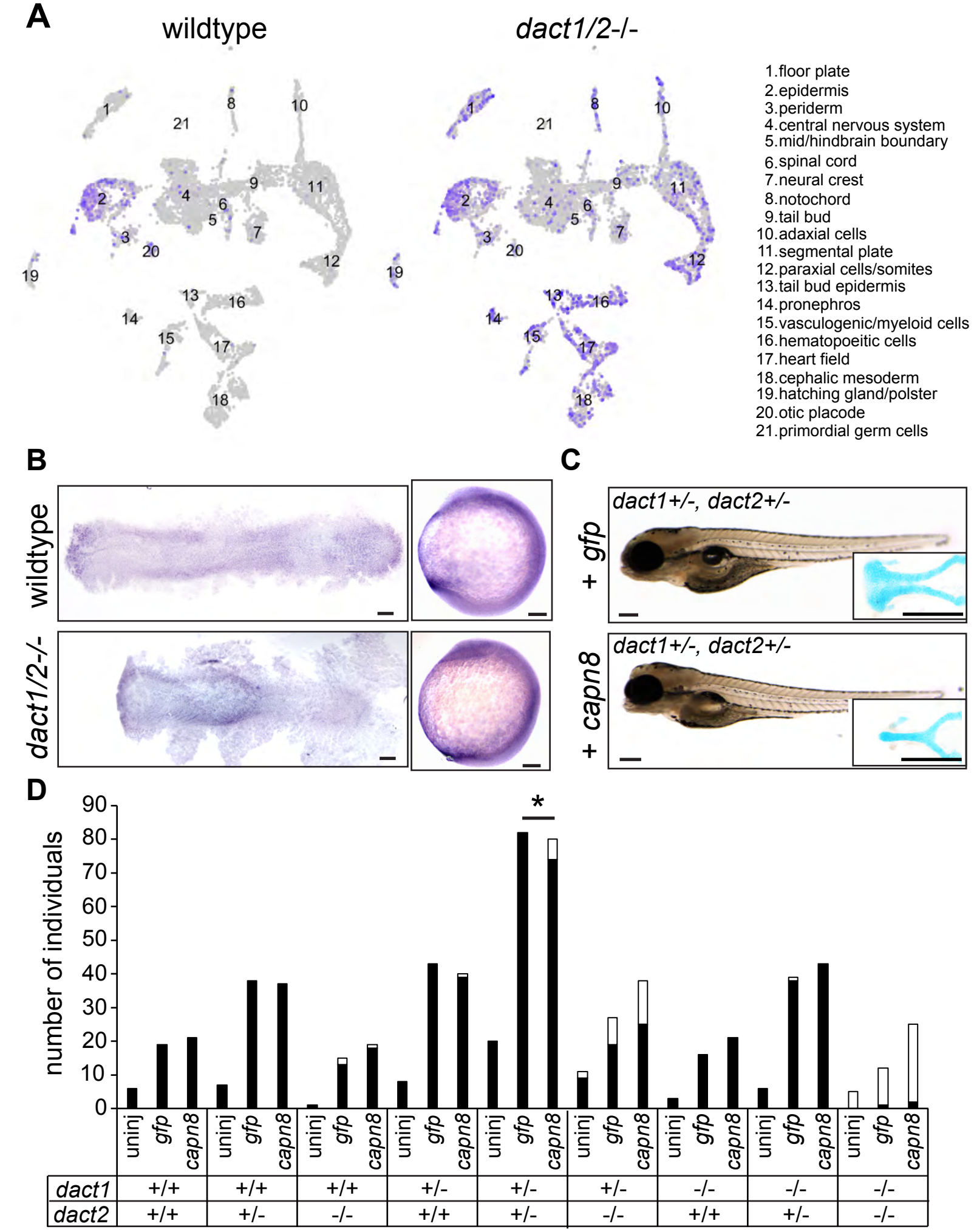
A
wildtype
dact1/2-/-
1.floor plate
2.epidermis
3.periderm
4.central nervous system
5.mid/hindbrain boundary
6.spinal cord
7.neural crest
8.notochord
9.tail bud
10.adaxial cells
11.segmental plate
12.paraxial cells/somites
13.tail bud epidermis
14.pronephros
15.vasculogenic/myeloid cells
16.hematopoeitic cells
17.heart field
18.cephalic mesoderm
19.hatching gland/polster
20.otic placode
21.primordial germ cells
B
wildtype
dact1/2-/-
C
dact1+/-, dact2+/-
+ gfp
dact1+/-, dact2+/-
+ capn8
D
number of individuals
0
10
20
30
40
50
60
70
80
90
*
uninj
gfp
capn8
dact1
+/+
+/+
+/+
+/-
+/-
+/-
-/-
-/-
-/-
dact2
+/+
+/-
-/-
+/+
+/-
-/-
+/+
+/-
-/-

Figure S1

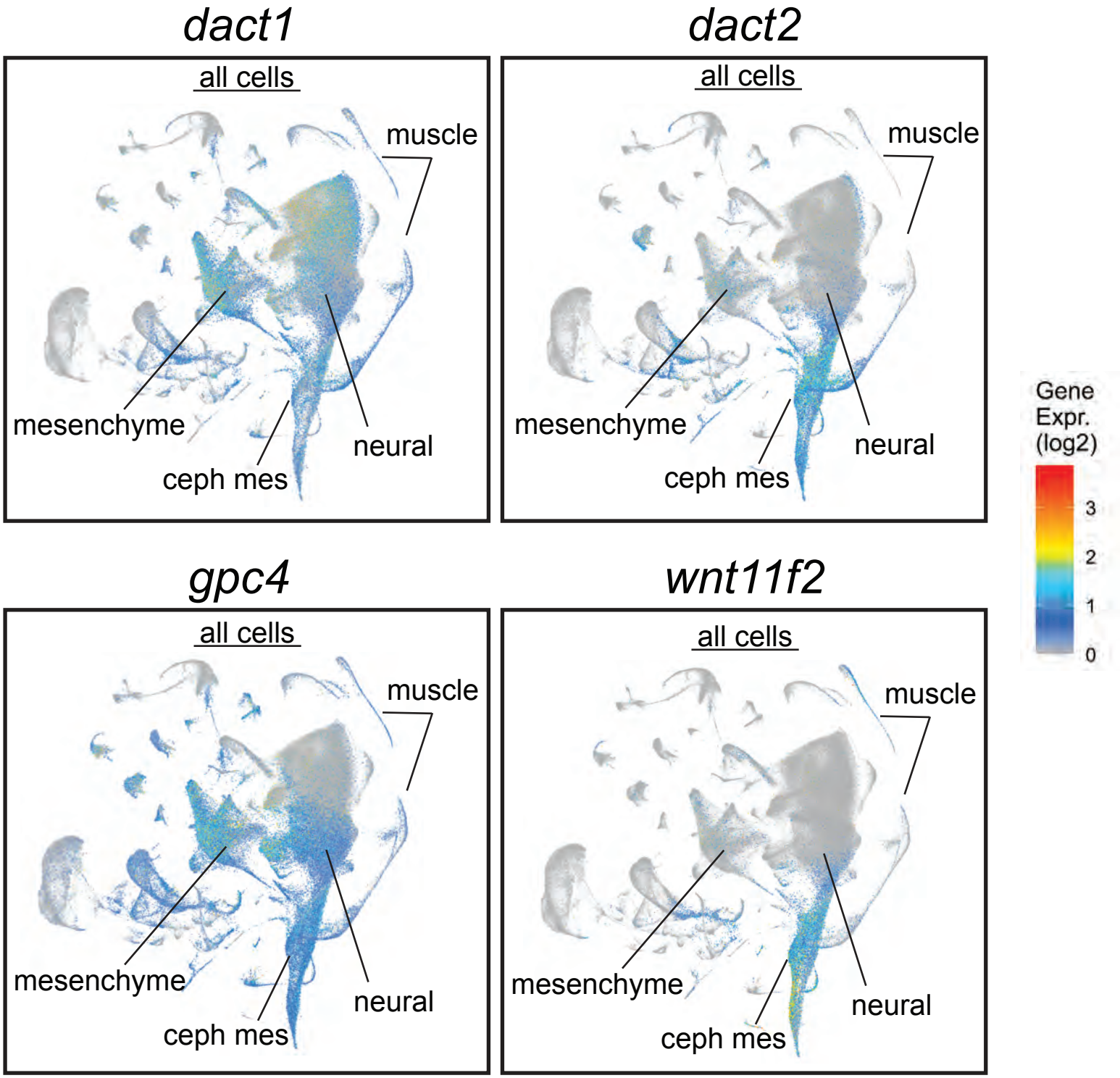
dact1
all cells
muscle
mesenchyme
neural
ceph mes
dact2
all cells
muscle
mesenchyme
neural
ceph mes
gpc4
all cells
muscle
mesenchyme
neural
ceph mes
wnt11f2
all cells
muscle
mesenchyme
neural
ceph mes
Gene Expr. (log2)
3
2
1
0

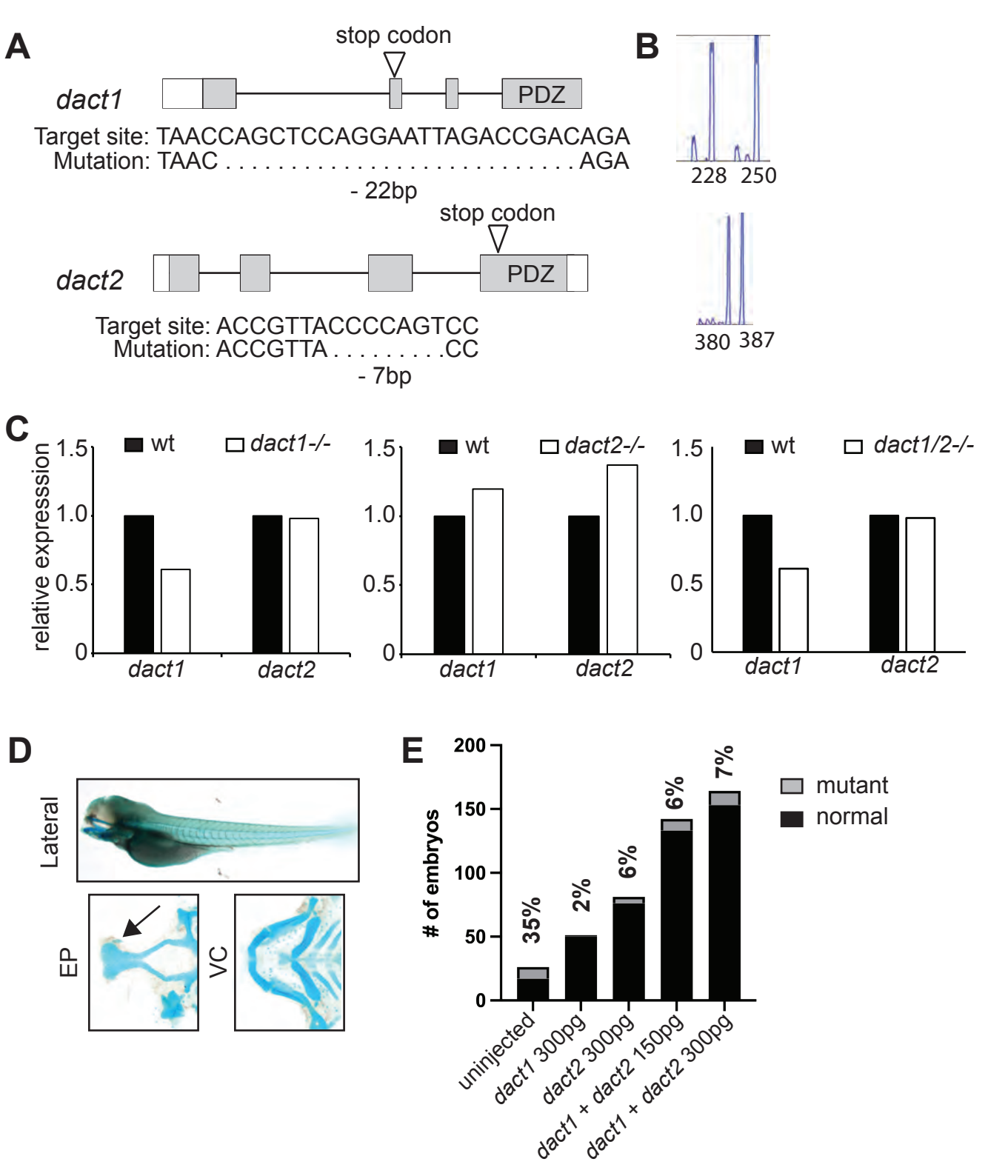
A
stop codon
dact1
PDZ
Target site: TAACCAGCTCCAGGAATTAGACCGACAGA
Mutation: TAAC . . . . . AGA
- 22bp
stop codon
dact2
PDZ
Target site: ACCGTTACCCCAGTCC
Mutation: ACCGTTA CC
- 7bp
B
228 250
380 387
C
relative expresssion
1.5
1.0
0.5
0
wt
dact1-/-
dact1
dact2
wt
dact2-/-
dact1
dact2
wt
dact1/2-/-
dact1
dact2
D
Lateral
EP
VC
E
# of embryos
200
150
100
50
0
35%
2%
6%
6%
7%
mutant
normal
uninjected
dact1 300pg
dact2 300pg
dact1 + dact2 150pg
dact1 + dact2 300pg

Figure S3

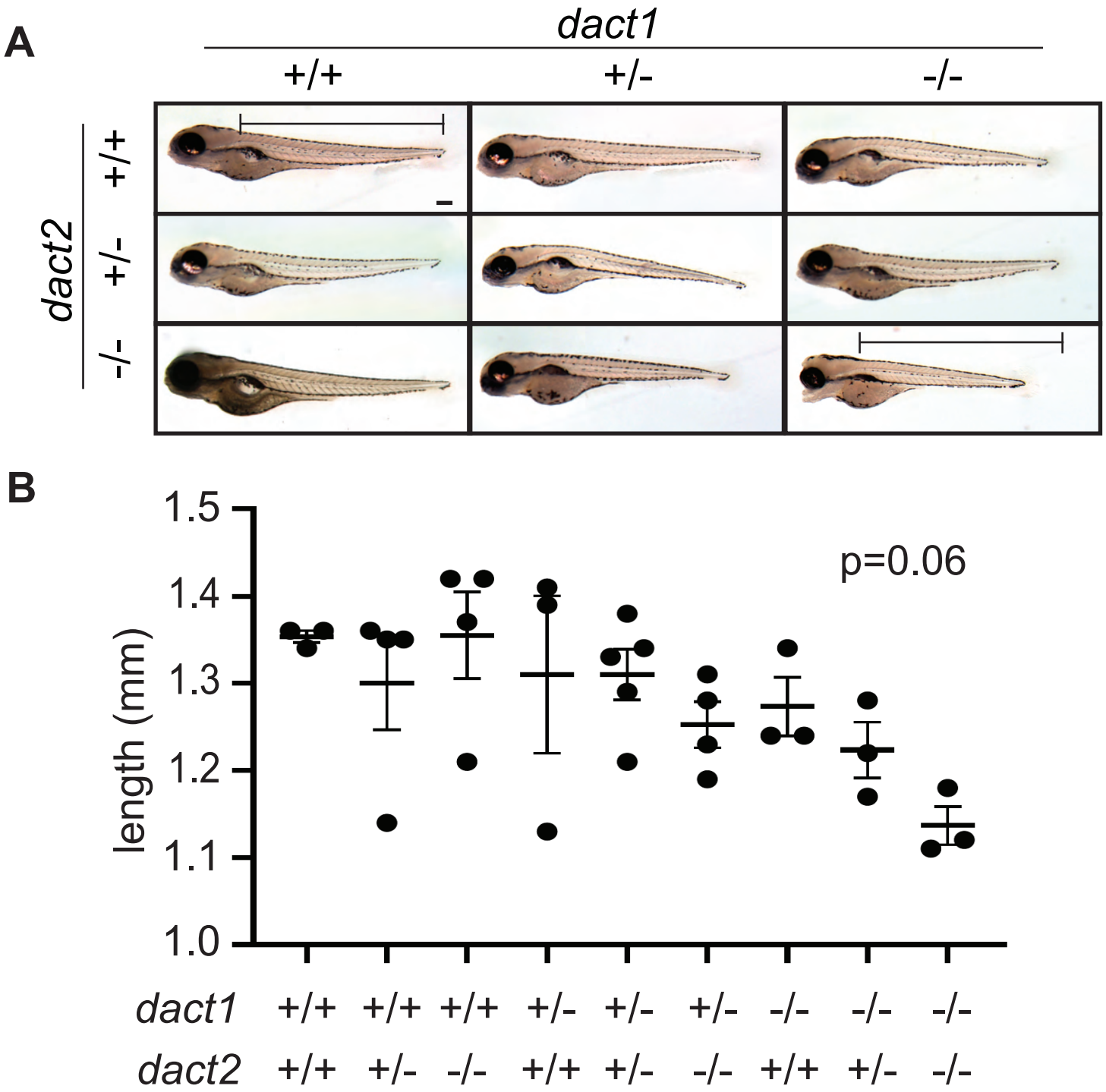

Figure S4

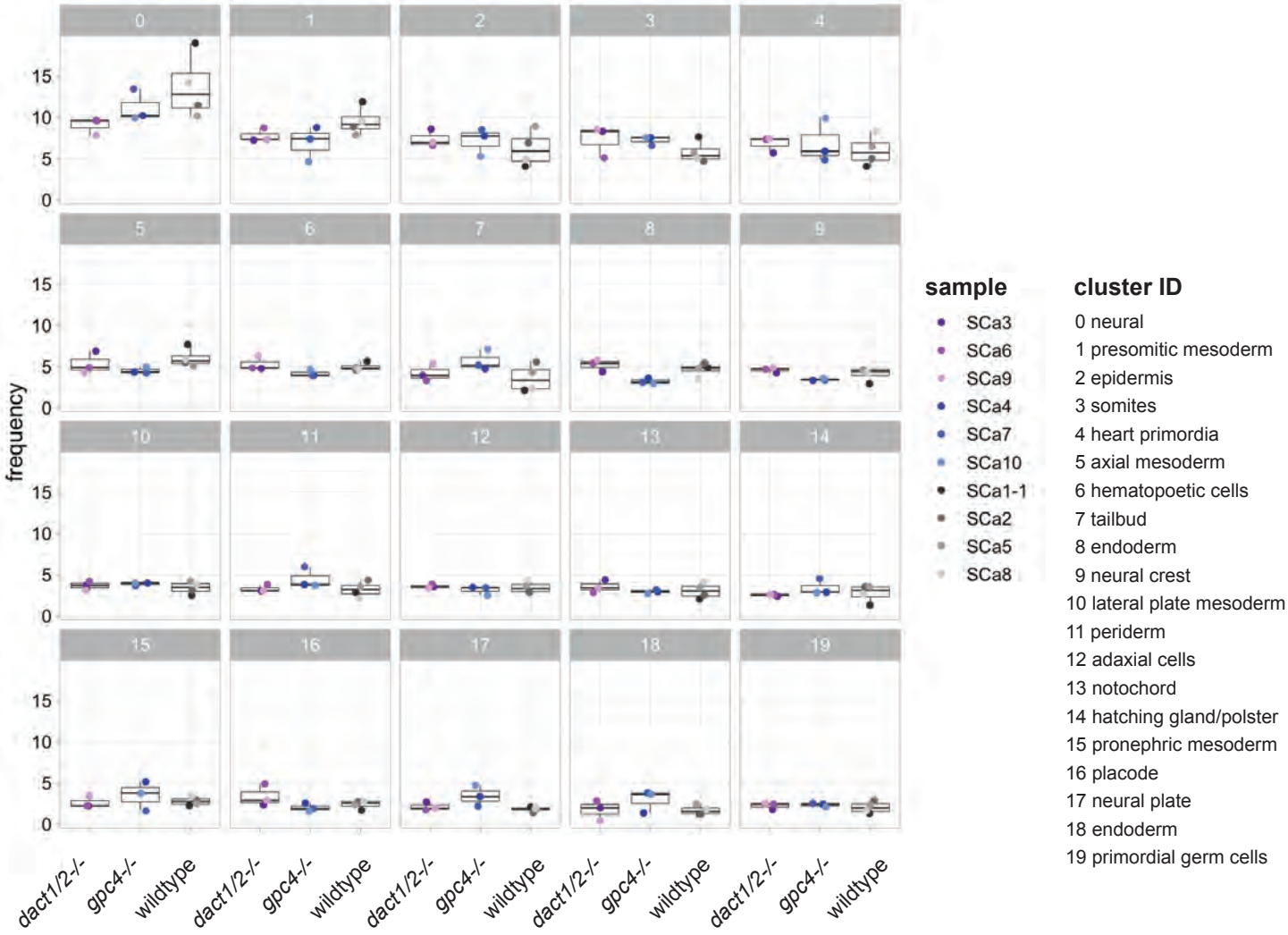
frequency
0
1
2
3
4
5
6
7
8
9
10
11
12
13
14
15
16
17
18
19
dact1/2-/-
gpc4-/-
wildtype
sample
SCa3
SCa6
SCa9
SCa4
SCa7
SCa10
SCa1-1
SCa2
SCa5
SCa8
cluster ID
0 neural
1 presomitic mesoderm
2 epidermis
3 somites
4 heart primordia
5 axial mesoderm
6 hematopoetic cells
7 tailbud
8 endoderm
9 neural crest
10 lateral plate mesoderm
11 periderm
12 adaxial cells
13 notochord
14 hatching gland/polster
15 pronephric mesoderm
16 placode
17 neural plate
18 endoderm
19 primordial germ cells

Figure S5

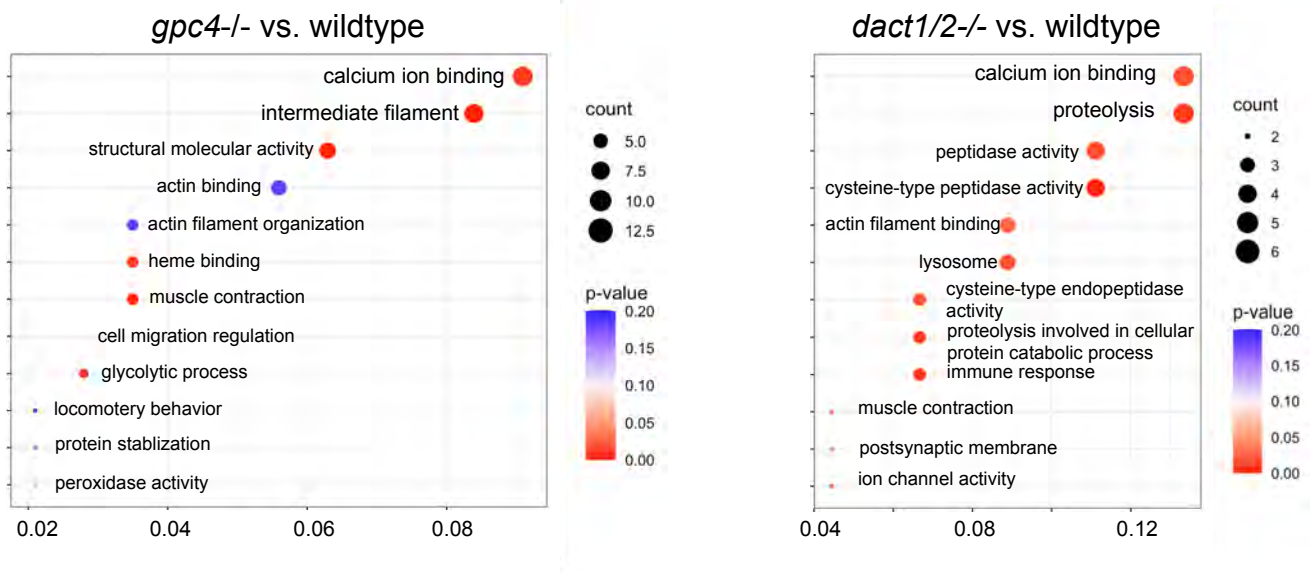
gpc4-/- vs. wildtype
calcium ion binding
intermediate filament
structural molecular activity
actin binding
actin filament organization
heme binding
muscle contraction
cell migration regulation
glycolytic process
locomotery behavior
protein stablization
peroxidase activity
0.02
0.04
0.06
0.08
count
5.0
7.5
10.0
12.5
p-value
0.20
0.15
0.10
0.05
0.00
dact1/2-/- vs. wildtype
calcium ion binding
proteolysis
peptidase activity
cysteine-type peptidase activity
actin filament binding
lysosome
cysteine-type endopeptidase activity
proteolysis involved in cellular protein catabolic process
immune response
muscle contraction
postsynaptic membrane
ion channel activity
0.04
0.08
0.12
count
2
3
4
5
6
p-value
0.20
0.15
0.10
0.05
0.00